university of groningen / faculty of science and engineering / Physics: Quantum Universe

2DEV Investigations of Dimers

Master Thesis

Physics: Quantum Universe
September 2022

by

G.A.H. ten Hoven
S2741261

Supervisor/First Examiner:

prof. dr. T.L.C. Jansen

Second Examiner:

prof. dr. M.S. Pchenitchnikov

It's the job that's never started, as takes longest to finish.

- Samwise Gamgee's Gaffer,

The Lord of the Rings, J.R.R. Tolkien

Abstract

Light harvesting in photosynthetic systems is one of the fundamental processes of life on Earth and is not understood fully. Not only is this mechanism worth studying for its own sake, understanding it might also inspire industrial light harvesting systems. In recent decades, investigations using multidimensional spectroscopy, notably 2DES and 2DIR, have improved our understanding of common light harvesting molecular systems. An essential process in light harvesting is energy (exciton) transport, which recent works have demonstrated involves vibronic coupling types. Moreover, vibronic couplings are potentially important in other systems such as organic photovoltaics and organic thermo-electrics.

In recent years a new 2D spectroscopy, 2DEV, has emerged that combines infrared and visible wavelength ranges, which is especially suitable for investigating vibronic activity, as it directly probes couplings between vibrations and electronic states and is therefore better suited than e.g. 2DES for studying such interactions. This work aims to contribute to the theoretical underpinnings needed to interpret 2DEV experiment results by verifying recent theoretical investigations and expanding thereon. Specifically, a homo- and heterodimer that feature Franck-Condon and/or Herzberg-Teller vibronic couplings are investigated by simulating 2DEV spectra. It is found that the different dimers have their unique features in the 2DEV spectra, which can be understood to some degree. It is also found for the heterodimer that specific 2DEV peaks might be discerned by changing the polarisations of the laser setup used, for non-zero dimer angles.

Keywords: Light harvesting systems, photosynthesis, exciton transport, multidimensional spectroscopy, 2DEV, NISE, double sided Feynman diagrams, Holstein Model, vibronic coupling, Franck-Condon, Herzberg-Teller

Contents

Chapter 1

Introduction

1.1 Introduction

It is important to understand the quantum mechanical phenomena underlying energy transport when it comes to understanding for instance natural light harvesting systems and possibly creating artificial light harvesting systems, such as organic photovoltaics [1]. It has been demonstrated that vibronic coupling, the mixing of vibrational and electronic degrees of freedom, plays an important role in energy transfer on a quantum level. Both intermolecular [2] and intramolecular [3] couplings are important here. The overall goal of this thesis is to shed light on this problem from the perspective of multi-dimensional spectroscopy.

Multidimensional spectroscopy has been used before to investigate systems featuring vibronic coupling. Specifically two-dimensional electronic spectroscopy (2DES) [4] combines electromagnetic pulses that change the electronic state of the system. Additionally, two-dimensional infrared (2DIR) spectroscopy combining pulses that change the system's vibrational state, has also been used to investigate vibronic coupling [5]. Two-dimensional electronic vibrational (2DEV) spectroscopy is a relatively new technique that combines the frequency regimes of the aforementioned two methods. Hence 2DEV directly probes the couplings between electronic and vibrational states in a way that 2DES and 2DIR do not.

While 2DIR and 2DES can also probe vibronic activity, 2DEV involves both the electronic and vibrational transition dipole moments of the investigated system, allowing for weak transitions that may not be apparent in either 2DES or 2DIR to become more visible in 2DEV [5]. Vibronic activity also manifests itself in linear absorption spectra, but different coupling types are not as distinguishable in that type of spectroscopy [6].

2DEV, first proposed in 2014 [7], has been used to investigate the correlation of nuclear and electronic degrees of freedom [5] in a more direct way. This is essentially achieved by first exciting the electronic degrees of the sample and then probing the effect on the vibrational degrees. Moreover, 2DEV has been used to investigate ultrafast excitonic transfer [8].

Few research groups so far have performed 2DEV investigations (theory and experiment), starting with the experiment on a laser dye [7] and later with the experiment on the vibronic coupling in high frequency vibrational modes [9] and on intramolecular vibrational and charge-transfer dynamics [10].

Theoretical investigations of 2DEV spectroscopy on vibronically coupled systems also include the study of systems evolving according to classical trajectories [11] and a near analytical study of strongly vibronically coupled systems [12]. Recent experimental 2DEV investigations include a study of Chlorophyll a and b [13] and the probing of relaxation dynamics in β-Apo-8'-carotenal [14].

Comparisons have been made between theory and experiment on 2DEV investigations of conical intersections [15], of center line slope evolution [16], vibronic couplings in a solar cell dye [17], of polarisation selective spectra [18, 19]. 2DEV has been featured in a textbook on multidimensional spectroscopy [20] and even a 3DEV investigation has been done [21].

2DEV spectroscopy is therefore still a relatively new technique that has added value compared to e.g. 2DIR or 2DES for investigating vibronic phenomena. In this work, three goals are set in order contribute to the theoretical underpinnings of 2DEV: 1) verify recent theoretical 2DEV investigations on a heterodimer [6], 2) expand a bit on those results by including laser polarisation in the simulations and 3) simulate 2DEV spectra for a homodimer [22] that has not yet been investigated with 2DEV.

The heterodimer features two types of vibronic coupling: Franck-Condon (FC) coupling and Herzberg-Teller (HT) coupling, both of which are quite 'weak' in that system. On the other hand, the homodimer features only 'strong' FC coupling, giving rise to uneasily interpretable transitions between vibronically mixed states. Thus while both systems are dimers, they have different character and are expected to have different 2DEV signatures.

The remainder of this thesis is structured as follows. In Chapter 2 the relevant physics is introduced, most notably the general definitions of the dimers' Hamiltonians and the setup of the 2DEV spectra calculations via perturbation theory. The physics described in that Chapter is translated to computer code, an overview of which is given in Chapter 3. With that code, some previous results on the heterodimer were verified and a few new things were calculated for both dimer types, which is presented in Chapter 4. A brief discussion on the uncertainty in these calculations and interpretation of the results is given in Chapter 5. The conclusion is given in Chapter 6. Finally, the Appendix contains figures illustrating specific points made in Chapter 4 and calculation details.

Chapter 2

Theory

In this section, the description of the investigated hetero- and homodimer systems is given along with the outline of the mathematical procedure to calculate 2DEV spectra on these systems.

2.1 System definitions

The first thing to outline is the description of the systems studied in this work. The mathematical construct outlined here is the so called Holstein Hamiltonian. It involves multiple 'sites' that each represent a chromophore. These sites each feature multiple electronic states. An electronic excitation on such a site (combined with an electron *hole* elsewhere) is called an 'exciton', a quasiparticle. States that have an electronic excitation on different sites can be coupled via electric dipole-dipole coupling. This work considers *dimer* systems, having two sites. Hence only nearest neighbour coupling need be considered.

The total system can be in an electronically excited state: once excited or multiple excited, though only 'once excited states' are included in this work, as that is sufficient for basic 2DEV investigations. Such an excited state can be referred to as the *excited manifold*. A 'manifold', because the electronic states are further divided in various sub-states: vibrational excitations. Depending on the precise formulation, a site can feature multiple vibrational modes that each can accommodate a different number of vibrational quanta and that each can have a different oscillator frequency.

Each of these vibrational modes can feature their own unique vibronic coupling activity types and strengths. Two considered in this work [6] are 1) Franck-Condon activity, which is *intramolecular*, involving electronic and vibrational transitions on a single site and 2) Herzberg-Teller activity, which is intermolecular, involving electronic transitions on two sites and vibrational transitions on a single site. Below, these concepts are mathematically defined, based on Refs. [6, 23]. Further sources for this section are Refs. [24–26]

2.1.1 Homodimer Hamiltonian

The Hamiltonian presented in Ref. [23] reads as follows,

$$H(t) = \epsilon_1(t)c_1^\dagger c_1 + \epsilon_2(t)c_2^\dagger c_2 + J(c_1^\dagger c_2 + c_2^\dagger c_1) \tag{2.1}$$

$$+ \omega_0 b_1^\dagger b_1 + \omega_0 b_2^\dagger b_2 + \omega_0 \sum_{n=1,2} c_n^\dagger c_n[\lambda(b_n^\dagger + b_n) + \lambda^2], \tag{2.2}$$

where the first three terms describe the electronic excitation (operators c) and interaction (via the coupling J). This represents a dimer that has fluctuating exciton energies $\epsilon_1(t)$ and $\epsilon_2(t)$. The last three terms describe the vibrational excitations (operators b_i) for the two separate sites and the vibronic coupling (Franck-Condon activity) via the Huang-Rhys factor λ^2. The specific numerical values used in this model are given in Appendix B.

2.1.2 Heterodimer Hamiltonian

The Hamiltonian presented in Ref. [6] reads as follows. The electronic part is given by

$$H_S = (h_A^g + h_B^g)\left|G\right\rangle\left\langle G\right| + \tag{2.3}$$

$$(h_A^e + h_B^g + \epsilon)\left|A\right\rangle\left\langle A\right| + \tag{2.4}$$

$$(h_A^g + h_B^e + \Delta E + \epsilon)\left|B\right\rangle\left\langle B\right| + \tag{2.5}$$

$$J(\left|A\right\rangle\left\langle B\right| + \left|B\right\rangle\left\langle A\right|), \tag{2.6}$$

which describes the energies of electronic ground state ($\left|G\right\rangle\left\langle G\right|$), the electronic excitations on either site A or B ($\left|A\right\rangle\left\langle A\right|$, $\left|B\right\rangle\left\langle B\right|$) and the dipole-dipole coupling between these excited states ($\left|A\right\rangle\left\langle B\right|+h.c.$). The average energy difference between the ground and excited manifold is given by ϵ. The excitonic gap is denoted by ΔE and represents the energy difference between the electronic excitations on either site. The specific numerical values of the Hamiltonian parameters are found in Appendix A.

Each of the terms in Eq. (2.6) denotes an electronic states that have vibronic substructure, encompassed in the vibrational Hamiltonians h_I^i. These sub-Hamiltonians are site and electronic manifold dependent, given in Ref. [6] by

$$h_I^i = \frac{\hbar\omega_{I,i,f}}{2}\left[p_{I,f}^2 + \left(q_{I,f} - \delta_{ie}\sqrt{2S_f}\right)^2\right] + \tag{2.7}$$

$$\delta_{IA}\frac{\hbar\omega_{I,i,s}}{2}\left[p_{I,s}^2 + \left(q_{I,s} - \delta_{ie}\sqrt{2S_s}\right)^2\right], \tag{2.8}$$

where index I denotes either site A or B, the index i denotes whether the site is in the electronically excited or ground state: (δ_{ie} is one if electronically excited), the subscripts s and f denote the 'slow' or 'fast' vibrational mode (later captured in the index α). The oscillators' frequencies ($\omega_{I,i,\alpha}$) are site, manifold and mode dependent. The ground manifold modes are harmonic oscillators and the

excited manifold modes are displaced harmonic oscillators, where the displacement is characterised by the Huang-Rhys factor, here denotes as S_α. The δ_{ie} denotes that the displacement only occurs in the excited electronic state. This displacement gives rise to a coupling between vibrational states of differing quanta, which is Franck-Condon coupling[6].

Now this vibrational hamiltonian is rewritten to the form that is actually implemented in this work. Combining the two modes s and f in one index α, Eq. (2.8) can be written as

$$h^i_{I,\alpha} = \frac{\hbar\omega_{I,i,\alpha}}{2}\left[p^2_{I,i,\alpha} + \left(q_{I,i,\alpha} \pm \delta_{ie}\sqrt{2S_\alpha}\right)^2\right], \tag{2.9}$$

where a '$\pm$' is substituted in order to track where this minus sign ends up (the physics is independent of the sign of this displacement anyway). Now substitute the following definitions of the momentum and position operators: $\hat{p} = i(\hat{a}^\dagger - \hat{a})/\sqrt{2}$, $\hat{q} = (\hat{a}^\dagger + \hat{a})/\sqrt{2}$, yielding

$$h^i_{I,\alpha} = \frac{\hbar\omega_{I,i,\alpha}}{2}\left[(i(\hat{a}^\dagger_{I,\alpha} - \hat{a}_{I,\alpha})/\sqrt{2})^2 + \left((\hat{a}^\dagger_{I,\alpha} + \hat{a}_{I,\alpha})/\sqrt{2} \pm \delta_{ie}\sqrt{2S_\alpha}\right)^2\right] \tag{2.10}$$

$$= \frac{\hbar\omega_{I,i,\alpha}}{2}\Big[-(\hat{a}^\dagger_{I,\alpha}\hat{a}^\dagger_{I,\alpha} - \hat{a}^\dagger_{I,\alpha}\hat{a}_{I,\alpha} - \hat{a}_{I,\alpha}\hat{a}^\dagger_{I,\alpha} + \hat{a}_{I,\alpha}\hat{a}_{I,\alpha})/2+ \tag{2.11}$$

$$\left((\hat{a}^\dagger_{I,\alpha}\hat{a}^\dagger_{I,\alpha} + \hat{a}^\dagger_{I,\alpha}\hat{a}_{I,\alpha} + \hat{a}_{I,\alpha}\hat{a}^\dagger_{I,\alpha} + \hat{a}_{I,\alpha}\hat{a}_{I,\alpha})/2 \pm 2(\hat{a}^\dagger_{I,\alpha} + \hat{a}_{I,\alpha})\delta_{ie}\sqrt{2S_\alpha}/\sqrt{2} + 2\delta_{ie}S_\alpha\right)\Big] \tag{2.12}$$

$$= \frac{\hbar\omega_{I,i,\alpha}}{2}\Big[-(\cancel{\hat{a}^\dagger_{I,\alpha}\hat{a}^\dagger_{I,\alpha}} - \hat{a}^\dagger_{I,\alpha}\hat{a}_{I,\alpha} - \hat{a}_{I,\alpha}\hat{a}^\dagger_{I,\alpha} + \cancel{\hat{a}_{I,\alpha}\hat{a}_{I,\alpha}})/2+ \tag{2.13}$$

$$\left((\cancel{\hat{a}^\dagger_{I,\alpha}\hat{a}^\dagger_{I,\alpha}} + \hat{a}^\dagger_{I,\alpha}\hat{a}_{I,\alpha} + \hat{a}_{I,\alpha}\hat{a}^\dagger_{I,\alpha} + \cancel{\hat{a}_{I,\alpha}\hat{a}_{I,\alpha}})/2 \pm 2(\hat{a}^\dagger_{I,\alpha} + \hat{a}_{I,\alpha})\delta_{ie}\sqrt{S_\alpha} + 2\delta_{ie}S_\alpha\right)\Big] \tag{2.14}$$

$$= \frac{\hbar\omega_{I,i,\alpha}}{2}\left[\hat{a}^\dagger_{I,\alpha}\hat{a}_{I,\alpha} + \hat{a}_{I,\alpha}\hat{a}^\dagger_{I,\alpha} \pm 2(\hat{a}^\dagger_{I,\alpha} + \hat{a}_{I,\alpha})\delta_{ie}\sqrt{S_\alpha} + 2\delta_{ie}S_\alpha\right] \tag{2.15}$$

$$= \frac{\hbar\omega_{I,i,\alpha}}{2}\left[2\hat{a}^\dagger_{I,\alpha}\hat{a}_{I,\alpha} + 1 \pm 2(\hat{a}^\dagger_{I,\alpha} + \hat{a}_{I,\alpha})\delta_{ie}\sqrt{S_\alpha} + 2\delta_{ie}S_\alpha\right] \tag{2.16}$$

$$= \hbar\omega_{I,i,\alpha}\left[\hat{a}^\dagger_{I,\alpha}\hat{a}_{I,\alpha} \pm (\hat{a}^\dagger_{I,\alpha} + \hat{a}_{I,\alpha})\delta_{ie}\sqrt{S_\alpha} + \delta_{ie}S_\alpha\right] + \frac{\hbar\omega_{I,i,\alpha}}{2} \tag{2.17}$$

$$= \hbar\omega_{I,i,\alpha}\left[N_{I,\alpha} \pm (\hat{a}^\dagger_{I,\alpha} + \hat{a}_{I,\alpha})\delta_{ie}\sqrt{S_\alpha} + \delta_{ie}S_\alpha\right] + \frac{\hbar\omega_{I,i,\alpha}}{2} \tag{2.18}$$

where in Eq. (2.16) use was made of the following commutation relation: $[\hat{a}, \hat{a}^\dagger] = \hat{a}\hat{a}^\dagger - \hat{a}^\dagger\hat{a} = 1$. The number $N_{I,\alpha} = \hat{a}^\dagger_{I,\alpha}\hat{a}_{I,\alpha}$ counts the number of vibrational excitations in this site specific vibrational mode. When using the following Hamiltonian basis set that is defined by the ladder operators a,

$$\hat{a}^\dagger_{I,\alpha}\left|n_{I,\alpha}\right\rangle = \sqrt{n_{I,\alpha}+1}\left|n_{I,\alpha}+1\right\rangle \tag{2.19}$$

$$\hat{a}_{I,\alpha}\left|n_{I,\alpha}\right\rangle = \sqrt{n_{I,\alpha}}\left|n_{I,\alpha}-1\right\rangle \tag{2.20}$$

the Hamiltonian elements can easily be determined. The energies on the diagonal of this vibrational matrix are determined by

$$\left\langle n_{I,\alpha}\right| h_{I,i,\alpha}\left|n_{I,\alpha}\right\rangle = \hbar\omega_{I,i,\alpha}\left[N_{I,\alpha} + \delta_{ie}S_\alpha\right] + \frac{\hbar\omega_{I,i,\alpha}}{2}, \tag{2.21}$$

which denotes that the energy of a state is determined by the number of vibrational quanta in the oscillator compared to some reference energy. In addition, the displaced harmonic oscillators (in the excited electronic state) get an additional energy shift.

The coupling between vibrational site states is given by these off-diagonal matrix elements:

$$\langle m_{I,\alpha}|\, h_{I,i,\alpha}\, |n_{I,\alpha}\rangle = \pm\hbar\omega_{I,i,\alpha}\, \langle m_{I,\alpha}|\, (\hat{a}^\dagger_{I,\alpha} + \hat{a}_{I,\alpha})\delta_{ie}\sqrt{S_\alpha}\, |n_{I,\alpha}\rangle \tag{2.22}$$

$$= \pm\hbar\omega_{I,i,\alpha}\delta_{ie}\sqrt{S_\alpha}(\sqrt{n_{I,\alpha}+1}\, \langle m_{I,\alpha}\,|\, n_{I,\alpha}+1\rangle + \sqrt{n_{I,\alpha}}\, \langle m_{I,\alpha}\,|\, n_{I,\alpha}-1\rangle). \tag{2.23}$$

The term $\sqrt{n+1}\,\langle m\,|\,n+1\rangle$ is non-zero if $m = n+1$ while $\sqrt{n}\,\langle m\,|\,n-1\rangle$ is non-zero if $m = n-1$. Hence these two terms can be combined as:

$$\langle m_{I,\alpha}|\, h_{I,i,\alpha}\, |n_{I,\alpha}\rangle = \pm\hbar\omega_{I,i,\alpha}\delta_{ie}\delta_{1\Delta}\sqrt{S_\alpha}\sqrt{\max(n_{I,\alpha}, m_{I,\alpha})}, \tag{2.24}$$

where use is made of the orthonormality of the basis states and $\Delta = |n_{I,\alpha} - m_{I,\alpha}|$ denotes the absolute difference between the number of vibrational quanta in this vibrational mode, at this site. In other words: this term is only non-zero for states that differ by a single quantum. The function $\max(n, m)$ gives the maximum of the two numbers n and m. This expression for the coupling is easily translated to computer code.

2.1.3 Comparison of Hamiltonian forms

Now if we compare the vibrational/vibronic parts of both the Hamiltonians in Eqs. (2.2 and 2.9), we find

$$h_{\text{homo}} = \omega_0 \sum_{n=1,2} b^\dagger_n b_n + c^\dagger_n c_n[\lambda(b^\dagger_n + b_n) + \lambda^2] \tag{2.25}$$

$$h_{\text{hetero}} = \hbar\omega_{I,i,\alpha}\left[\hat{a}^\dagger_{I,\alpha}\hat{a}_{I,\alpha} + \delta_{ie}\left(\pm\sqrt{S_\alpha}(\hat{a}^\dagger_{I,\alpha} + \hat{a}_{I,\alpha}) + S_\alpha\right)\right] + \frac{\hbar\omega_{I,i,\alpha}}{2}. \tag{2.26}$$

These expressions contain the same essential physics. Given that only one electronic excitation is included in these dimer systems, δ_{ie} is equivalent to $c^\dagger_n c_n$, which counts the number of electronic excitations. However, h_{hetero} is slightly more general: is has multiple vibrational modes per site with frequencies that are mode and site specific, which needs to be taken into account when counting vibrational quanta. Additionally, this yields mode specific Huang-Rhys factors. Note that S_α corresponds to λ^2.

In h_{homo} the term $\hbar\omega_0/2$ (not shown) can be omitted as it is a general constant in that Hamiltonian. Note, however that $\frac{\hbar\omega_{I,i,\alpha}}{2}$ is simply a reference energy: the energies of the vibrational states are taken in reference to electronic states.

2.1.4 Vibronic Coupling

The mentioned displacement of the harmonic oscillators in the excited electronic manifold gives rise to Franck-Condon activity. Practically this means that an electronic excitation on a certain

site can give rise to an additional vibrational excitation on the same site, since those states are *coupled*. When two sites are electronically coupled, the combination of electronic and vibrational coupling gives rise to *vibronic activity*.

Another effect incorporated in the investigations of the heterodimer[6] is the so called Herzberg-Teller coupling, which is a non-Condon effect: it involves a nuclear coordinate dependence of the electronic coupling between sites in the Holstein model.

This is an effect that involves a vibrational transition accompanied by a 'move' of the exciton from one site to another. The most simple case of this phenomenon is described for a single site, where its nuclear coordinate $q_{A,s}$ influences electronic coupling with neighbouring sites, as in

$$J = J(q_{A,s}) = J_0(1 + \sqrt{2}\eta q_{A,s}), \tag{2.27}$$

where the '1' represents dipole-dipole coupling between the electronic dipoles of the two sites in the dimer. The Herzberg-Teller coupling strength is characterised by the parameter η. When placed in the context of the Hamiltonian defined in Eq. (2.6), the nuclear coordinate $q_{A,s}$ dependence implies the coupling of two states that differ in one vibrational quantum on the low energy mode at site A and that differ in location of the exciton. (Recall that the nuclear coordinate can be written in ladder operator notation: $\hat{q} = (\hat{a}^\dagger + \hat{a})/\sqrt{2}$.)

Since the dipole-dipole coupling in Eq. (2.27) involves the same physical dipoles that cause transitions between states, the Herzberg-Teller activity is also explicitly present in the electronic transition dipole matrices, described in the next section. This is in contrast with the Franck-Condon activity, which is 'fully' captured in the system Hamiltonian.

2.1.5 Dipole matrix definitions

The interactions of the external electromagnetic fields with the system (dimer) is described by transition dipole matrices (TDMs). The definitions of these TDMs is such that within the site basis the electronic TDM can cause a transition between states that differ a single quantum on a single site in the electronic part of the Hamiltonian. Similarly, the vibrational TDM is such that it can cause a transition between states that differ a single quantum in the on-resonance vibrational mode on a single site in site basis.

Electric TDM

The electronic TDM can be split in site specific matrices, as in

$$\mu_{el} = \mu_A + \mu_B, \tag{2.28}$$

where A and B describe the respective sites. These $\mu's$ can be expanded as

$$\mu_I = \mu_{I0}\left(1 + \delta_{IA}\sqrt{2}\eta q_{A,s}\right)(|I\rangle\langle G| + |G\rangle\langle I|), \tag{2.29}$$

which assumes non-zero value when combining the electronic ground state with a state being electronically excited on either site (I can be either A or B). The electronic TDM moment at site A takes a form similar to that in Eq. (2.27), because both equations are rooted in the same physical electric dipole and include Herzberg-Teller activity. Again, the parameter η specifies the strength of the Herzberg-Teller coupling on the low frequency vibrational mode at site A.

In order to arrive at the form implemented in this work, as in the previous section the equation $\hat{q}_{A,s} = (\hat{a}^\dagger_{A,s} + \hat{a}_{A,s})/\sqrt{2}$ is substituted, yielding

$$\langle m_{A,s}| \langle G| \mu_I |I\rangle |n_{A,s}\rangle = \langle m_{A,s}| \langle G| \mu_{I0} \left(1 + \delta_{IA}\sqrt{2}\eta q_{A,s}\right) (|I\rangle \langle G| + |G\rangle \langle I|) |I\rangle |n_{A,s}\rangle \tag{2.30}$$

$$= \langle m_{A,s}| \mu_{I0} \left(1 + \delta_{IA}\sqrt{2}\eta q_{A,s}\right) |n_{A,s}\rangle \tag{2.31}$$

$$= \langle m_{A,s}| \mu_{I0} \left(1 + \delta_{IA}\eta(\hat{a}^\dagger_{A,s} + \hat{a}_{A,s})\right) |n_{A,s}\rangle \tag{2.32}$$

$$= \mu_{I0} \left(\delta_{0\Delta} + \delta_{IA}\delta_{1\Delta}\eta\sqrt{\max(m_{A,s}, n_{A,s})}\right), \tag{2.33}$$

where $\Delta = |m_{A,s} - n_{A,s}|$, similar to the derivation done in Eq. (2.24). Hence there is a transition dipole value of μ_{I0} if there are is no quantum difference in the low vibrational mode state. There is a TDM value that depends on strength η, between states that have a single quantum difference in the low frequency mode at site A.

For the homodimer analysis, the Herzberg-Teller activity is simply excluded by setting η to zero.

Vibrational TDM

The vibrational TDM presented in Ref. [6] is simple in the sense that it only specifies transitions between states that differ a single quantum in the specified on-resonance modes. It can be split in site specific matrices, as in

$$\mu_{vib} = \mu_{A,f} + \mu_{B,f},$$

where $\mu_{I,f} = \sqrt{2}q_{I,f} |I\rangle \langle I|$. In this work however, in the excited electronic state we take the displacement of the on-resonance vibrational mode into account in the definition of the vibrational TDM, using

$$\mu_{I,f} = \sqrt{2}(q_{I,f} - d_{I,f}) |I\rangle \langle I| = \sqrt{2}(q_{I,f} - \delta_{ie}\sqrt{2S_f}) |I\rangle \langle I|,$$

where the displacement's definition is in line with that in Eq. (2.8). The vibrational TDM can be rewritten as

$$\begin{aligned}\mu_{vib} &= \sqrt{2}(q_{A,f} - \delta_{ie}\sqrt{2S_f}) |A\rangle \langle A| + \sqrt{2}(q_{B,f} - \delta_{ie}\sqrt{2S_f}) |B\rangle \langle B| \\ &= (\hat{a}^\dagger_{A,f} + \hat{a}_{A,f} - 2\delta_{ie}\sqrt{S_f}) |A\rangle \langle A| + (\hat{a}^\dagger_{B,f} + \hat{a}_{B,f} - 2\delta_{ie}\sqrt{S_f}) |B\rangle \langle B|,\end{aligned}$$

where again use was made of $(q = \hat{a}^\dagger + \hat{a})/\sqrt{2}$ and the fact that the on resonance modes at both sites get the same Huang-Rhys factor S_f. So the matrix element of μ_{vib} at e.g. exciton site B becomes

$$\langle m_{B,f}| \mu_{vib} |n_{B,f}\rangle = \langle m_{B,f}| (\hat{a}^\dagger_{B,f} + \hat{a}_{B,f} - 2\delta_{ie}\delta_{nm}\sqrt{S_f}) |n_{B,f}\rangle \tag{2.34}$$

$$= \langle m_{B,f}| (\delta_{1\Delta}\sqrt{\max(m_{B,f}, n_{B,f})} - 2\delta_{ie}\delta_{nm}\sqrt{S_f}) |n_{B,f}\rangle , \tag{2.35}$$

in line with the derivation of Eq. (2.24). The right term represents diagonal elements in the TDM: they correspond to a permanent dipole moment.

As seen, both the electronic and vibrational TDMs are split in site specific matrices. These can be combined geometrically to represent different dimer angles, as in

$$\mu_x = \sin(\theta)\mu_B \tag{2.36}$$

$$\mu_y = \mu_A + \cos(\theta)\mu_B, \tag{2.37}$$

which reflects that if the dimer angle is zero, the TDMs are parallel and that if the dimer angle is $\pi/2$, the TDMs are perpendicular. This expression is applied to both the electronic and vibrational TDMs, which are assumed parallel within each chromophore.

Bath Coupling

There are multiple approaches to implementing system-environment interactions in 2D spectra calculations. The environment is called a *bath*. Options include different approaches to the bath coupling, for instance by explicitly describing the bath in a *bath Hamiltonian* and coupling that Hamiltonian in specific ways to the investigated system[6]. Instead of that, in this work the bath is implemented by fluctuating Hamiltonian parameters, specifically the energy levels of the Hamiltonian in the homodimer, so called diagonal disorder, as in Refs. [23, 27]. This energy disorder is caused by interactions with the bath that are not made explicit: only the net effect on the energy levels is made explicit.

The calculation of the fluctuating energies is a Markovian process where the disorder is generated randomly in such a way that the correlation function of the disorder at two moments in time decays exponentially[23], as in

$$\langle \epsilon_n(t)\epsilon_n(t + \Delta t)\rangle = \sigma_n^2 e^{-\Delta t/t_c}, \tag{2.38}$$

where σ_n is the standard deviation of the fluctuation of the specified energy level and t_c is the correlation time. This type of disorder can be generated by random number generation and using the following expression[27], where the fluctuation at time $t + \Delta t$ depends on that at time t:

$$\delta\epsilon_n(t + \Delta t) = \delta\epsilon_n(t)e^{-\Delta t/t_c} + G(\sigma)\sqrt{1 - \exp(-2\Delta t/t_c)}, \tag{2.39}$$

where σ and t_c are as in Eq. (2.38) and $G(\sigma)$ is a random number from a normal distribution centered at zero with standard deviation σ. Using this expression a *bath trajectory* (or *realisation*) can be calculated for a single dimer. Three such trajectories are shown in Chapter 4, in Fig. 4.9. This type of bath implementation is also called the *overdamped Brownian oscillator oscillator model*.

The ensemble average of the collection of dimers will be calculated, which is done by summing the 2DEV response for each of the individual dimers. The fluctuations of the individual dimer energies will give rise to variations in the sinusoidal type response function corresponding to each, which in turn will cause a decay of the average response signal as function of the waiting times in the interaction process, as defined in the Feynman diagrams. The corresponding 'decay rates' in the respective time domains give rise to peak widths in the 2DEV spectra.

Also non-diagonal disorder could be incorporated, which means that the couplings between the system's states fluctuate, but that is not included in this work.

2.2 2DEV spectroscopy calculations

In this work, the systems outlined on the previous pages are investigated by calculating so called 'third order response functions'[24–26], specifically 2DEV response functions, which are well described in Refs. [5, 7, 20, 28]. A relatively short overview of these calculations, based on the cited works, is reproduced here.

Linear, or one dimensional spectroscopy involves the simple process where a system is excited by some electromagnetic pulse and then 'responds' after some time by emitting another. Multidimensional spectroscopy on the other hand, is based on a slightly more elaborate mechanism, i.e. pulse sequence: multiple pulses interact with the system, after which the system responds with a final pulse. The essence of multidimensional spectroscopy calculations is therefore to compute how a system evolves after interacting with n electromagnetic pulses and how it finally 'responds'. Two dimensional spectroscopy involves three pulses after which the system 'responds' with a final pulse.

The mechanism behind 2DEV spectroscopy is as follows. The system interacts with external electromagnetic fields in the specific order depicted in Fig. 2.1. In total, the system interacts four times with an electromagnetic field. The first two interactions happen in the 'electronic' part of the spectrum, while the second two interactions occur in the infrared part of the spectrum. The fourth pulse represents the system's response.

There are three time intervals between the four pulses. All three time intervals can be varied to investigate the system's time-dependent nature. The first and third time intervals are relevant for 2DEV spectroscopy: the two-dimensional Fourier transform of the system's response over these two time intervals represents the 2DEV spectrum. The second time interval can be varied in order to investigate so called 'beating' patterns, which represent how the system's 2DEV response evolves over the *waiting time*.

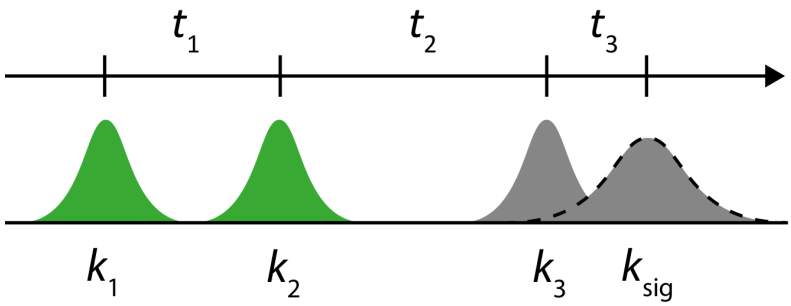

FIGURE 2.1: The sequence of laser pulses used in 2DEV spectroscopy, as depicted in Ref. [7]. The first two pulses are in the 'electronic' band of the spectrum, meaning they give rise to electronic (de-)excitations, while the second two are in the infrared part of the spectrum and give rise to vibrational (de-)excitations.

2.2.1 Polarisation of materials

On a classical scale, an interaction with an electromagnetic field can cause a polarisation within a material. This can be described by[26]

$$P = \epsilon_0(\chi^{(1)}E + \chi^{(2)}E^2 + \chi^{(3)}E^3 + \dots), \tag{2.40}$$

where P is the polarisation, $\chi(n)$ the n-th order susceptibility and E the electric field. First and third order are considered, not even orders, as those terms vanish for isotropic media, which is what we will consider.

The microscopic polarisation of a system (e.g. a single molecule) is given by $P(t) = \langle\psi(t)|\,\mu(t)\,|\psi(t)\rangle$, where ψ is the system's state and μ is the system's oscillating dipole. The macroscopic polarisation can be described by an ensemble average of those:

$$P(t) = \langle\langle\psi(t)|\,\mu(t)\,|\psi(t)\rangle\rangle_E\,, \tag{2.41}$$

where the subscript denotes the ensemble average. The interaction with external fields is described perturbatively, with the perturbative Hamiltonian being

$$W_I = -\vec{\mu}_I(t)\cdot\vec{E}(t) + \overleftrightarrow{\nu_I}\!:\vec{E}(t)\vec{E}(t) + \dots, \tag{2.42}$$

expressed as an electric multipole expansion, where the subscript I denotes interaction picture (explained later). Only the lowest order is considered here, while the quadrupole moment interactions and higher are not. As such, the interaction is described by an electronic transition dipole moment (TDM) that couples to the external electromagnetic field.

2.2.2 Evolution after external field interactions

The evolution of the system is governed by the Schrödinger equation, which in integral form is given by

$$|\psi(t)\rangle = |\psi(t_0)\rangle - \frac{i}{\hbar}\int_{t_0}^{t} d\tau_1 H(\tau_1)\,|\psi(\tau_1)\rangle\,, \tag{2.43}$$

described well in for instance Ref. [29]. The system's Hamiltonian can be described by

$$H(t) = H_0 + W(t), \tag{2.44}$$

where H_0 is the time independent Hamiltonian and $W(t)$ is the time dependent perturbation of this hamiltonian. Here[24] the perturbation describes the interaction of the system with the external light, which depends on time. The corresponding interaction potential is written as[24]

$$W(t) = -\vec{\mu}\cdot\vec{E}(t), \tag{2.45}$$

where $\vec{\mu}$ is the system's electric dipole. The solution to the Schrödinger equation for a time independent Hamiltonian reads

$$|\psi(t)\rangle = U(t,t_0)\,|\psi(t_0)\rangle\,, \tag{2.46}$$

where $U(t,t_0)$ is the time evolution operator, defined as

$$U(t,t_0) = \exp\left(-\frac{i}{\hbar}(t-t_0)H_0\right). \tag{2.47}$$

The expressions so far are in the so called *Schrödinger* picture, where the time evolution is expressed separate from the operators and wavefunctions. It is convenient to make a transformation to the *interaction* picture where the time evolution due to the time independent part of the Hamiltonian, H_0, is absorbed in the operators and wavefunctions. The Schrödinger equation is then solved perturbatively by considering the time dependent part of the Hamiltonian, $W(t)$ as the perturbation. An operator $\mathbf{M}_S(t)$ that exists in the Schrödinger picture is transformed to the interaction picture $\mathbf{M}_I(t)$ by

$$\mathbf{M}_I(t) = U(t,t_0)^\dagger \mathbf{M}_S(t) U(t,t_0), \tag{2.48}$$

with $U(t,t_0)$ is as in Eq. (2.47), containing the time independent part of the Hamiltonian, H_0. Similarly, a wavefunction is transformed as

$$|\psi_I(t)\rangle = U(t,t_0)^\dagger\,|\psi_S(t)\rangle\,. \tag{2.49}$$

. In the interaction picture, the Schrödinger equation reads

$$|\psi_I(t)\rangle = |\psi_I(t_0)\rangle - \frac{i}{\hbar}\int_{t_0}^{t} d\tau_1 W_I(\tau_1)\,|\psi_I(\tau_1)\rangle\,, \tag{2.50}$$

where the time evolution of the wavefunction is solely governed by the (time dependent) perturbation: the interaction part of the Hamiltonian. This equation can be solved in an iterative manner by substituting it into itself, yielding

$$|\psi_I(t)\rangle = |\psi_I(t_0)\rangle - \frac{i}{\hbar}\int_{t_0}^{t} d\tau W_I(\tau)\,|\psi_I(t_0)\rangle + \left(\frac{-i}{\hbar}\right)^2 \int_{t_0}^{t} d\tau_2 \int_{t_0}^{\tau_2} d\tau_1 W_I(\tau_2) W_I(\tau_1)\,|\psi_I(\tau_1)\rangle\,. \tag{2.51}$$

This procedure can be repeated an arbitrary number of times, yielding

$$|\psi_I(t)\rangle = |\psi_I(t_0)\rangle + \sum_{n=1}^{\infty}\left(\frac{-i}{\hbar}\right)^n \int_{t_0}^{t} d\tau_n \int_{t_0}^{\tau_n} d\tau_{n-1}\cdots\int_{t_0}^{\tau_2} d\tau_1 (W_I(\tau_n)W_I(\tau_{n-1})\ldots W_I(\tau_1))\,|\psi_I(t_0)\rangle\,. \tag{2.52}$$

The Hermitian conjugate of this equation is simple, as the W_I operators are Hermitian.

2.2.3 Response functions

As described in Eq. (2.40), a material is polarised in orders corresponding to the number of interactions with an external electric field. Using Eq. (2.41) we can write the macroscopic polarisation due to n interactions with an electric field. Using the interaction picture immediately gives[26]

$$P^{(n)}(t) = \sum_{m=0}^{m=n} \left\langle \left\langle \psi_I^{(n-m)}(t) \right| \mu_I(t) \left| \psi_I^{(m)}(t) \right\rangle \right\rangle_E , \tag{2.53}$$

where ϕ^m denotes the wavefunction of a system (dimer in this case) that has interacted m times with an external electric field. Note that $n-m$ and m add up to n, which means that the system responds to n interactions with an electric field, which can act on either the Bra or the Ket side of the final response operator $\mu_I(t)$, which gives rise to different Feynman diagram types. Solving this equation with various assumptions and for various parameters is at the heart of multidimensional spectroscopy.

Substituting Eq. (2.52) in Eq. (2.53) gives

$$P^{(n)}(t) = \int_{t_0}^{t} d\tau_m^K \int_{t_0}^{\tau_m^K} d\tau_{m-1}^K \cdots \int_{t_0}^{\tau_2^K} d\tau_1^K \int_{t_0}^{t} d\tau_{n-m}^B \int_{t_0}^{\tau_{n-m}^B} d\tau_{n-m-1}^B \cdots \int_{t_0}^{\tau_2^B} d\tau_1^B \sum_{m=0}^{m=n} \left(\frac{-i}{\hbar}\right)^m \left(\frac{i}{\hbar}\right)^{n-m} \tag{2.54}$$

$$\left\langle \langle \psi_I(t_0)| \left(W_I(\tau_1^B) \ldots W_I(\tau_{n-m-1}^B) W_I(\tau_{n-m}^B)\right) \mu_I(t) \left(W_I(\tau_m^K) W_I(\tau_{m-1}^K) \ldots W_I(\tau_1^K)\right) |\psi_I(t_0)\rangle \right\rangle_E , \tag{2.55}$$

where all the time coordinates τ_n^B and τ_n^K are dummy coordinates over which is integrated to solve the Schrödinger equation. Now invoke the interaction description $W_I(t) = -\vec{\mu}_I \cdot E(t)(t)$ yielding the following three line expression

$$P^{(n)}(t) = \int_{t_0}^{t} d\tau_m^K \int_{t_0}^{\tau_m^K} d\tau_{m-1}^K \cdots \int_{t_0}^{\tau_2^K} d\tau_1^K \int_{t_0}^{t} d\tau_{n-m}^B \int_{t_0}^{\tau_{n-m}^B} d\tau_{n-m-1}^B \cdots \int_{t_0}^{\tau_2^B} d\tau_1^B \sum_{m=0}^{m=n} \left(\frac{-i}{\hbar}\right)^m \left(\frac{i}{\hbar}\right)^{n-m} (-1)^n \tag{2.56}$$

$$\left\langle \langle \psi_I(t_0)| \left(\mu_I(\tau_1^B) \ldots \mu_I(\tau_{n-m-1}^B) \mu_I(\tau_{n-m}^B)\right) \mu_I(t) \left(\mu_I(\tau_m^K) \mu_I(\tau_{m-1}^K) \ldots \mu_I(\tau_1^K)\right) |\psi_I(t_0)\rangle \right\rangle_E \tag{2.57}$$

$$E(\tau_1^B) \ldots E(\tau_{n-m-1}^B) E(\tau_{n-m}^B) E(\tau_m^K) E(\tau_{m-1}^K) \ldots E(\tau_1^K), \tag{2.58}$$

where the factor $(-1)^n$ originates in the minus sign of the interaction potential $W_I(t)$. Now assume that the electric fields have delta shape envelope: $\vec{E}(\tau_i) \propto \delta(\tau_i)$, with the peaks occurring instantaneously at times $[t_1, t_2 \ldots t_n]$. The proportionality hides the electric field strengths. The intensities of the spectra calculated in this work are given in arbitrary units: what is investigated here is the 'spectral shape' and not the absolute intensities of the system's response. Hence a proportionality sign in introduced. This yields

$$P^{(n)}(t) \propto \sum_{m=0}^{m=n} \left(\frac{-i}{\hbar}\right)^m \left(\frac{i}{\hbar}\right)^{n-m} (-1)^n \tag{2.59}$$

$$\langle\langle\psi_I(t_0)| \left(\mu_I(t_1)\dots\mu_I(t_{n-m-1})\mu_I(t_{n-m})\right)\mu_I(t)\left(\mu_I(t_m)\mu_I(t_{m-1})\dots\mu_I(t_1)\right)|\psi_I(t_0)\rangle\rangle_E\,. \tag{2.60}$$

Note that $|\psi_I(t_0)\rangle = U^\dagger(t_0,t_0)\,|\psi(t_0)\rangle = I\,|\psi(t_0)\rangle = |\psi(t_0)\rangle$, which shows that all the time evolution is now contained in the transition dipole operators.

In Eq. (2.60), time is present in the following manner: it starts at t_0 at either end of the inner Bra-Ket product and reaches its highest value in the final transition dipole moment (TDM) $\mu_I(t)$. Hence the operators $\mu_I(t_n)\dots$ must be time-ordered on each respective side of the final TDM. For instance, if a single operator is on the Ket side of the final TDM, then any of the n number of μ_I's may take that position, while the other $n-1$ operators must be ordered in their unique time-ordered manner. This yields n unique operator orderings that all have a single μ_I on the Ket side of the final transition dipole moment. Similarly, there exist n unique operator orderings that have a single μ_I on the Bra side of the final transition dipole moment. Indeed these two sets of n orderings are each other's complex conjugate.

If two TDMs are placed on the Ket side of the final TDM, then these two operators have a unique time ordering, as do the remaining $n-2$ TDMs. Any two of the n TDMs may take these places, which means that $n(n-1)/2$ unique TDMs can take these spots; the division by two reflects that these two operators must be time ordered. So there exist $n(n-1)/2$ unique terms that have two TDMs on the Ket side of the final TDM. Again, there are $n(n-1)/2$ conjugate terms that have two TDMs on the Bra side of the final TDM.

This can be generalised to there being $\binom{n}{m} = n!/(m!(n-m)!)$ unique terms that have m TDMs on the Ket side of the final TDM, for an order n response. Hence each term labelled by m in Eq. (2.60) is constituted by $\binom{n}{m}$ different time ordered terms, which all adds up to 2^n terms. All these different orderings correspond to unique physical processes that can be represented by double sided Feynman diagrams. Specifically, 2DEV spectroscopy investigates the response of a system after it has interacted three times with an external electromagnetic field. Hence it is a third order response, featuring $2^3 = 8$ different Feynman diagrams (and their complex conjugates).

2.2.4 2DEV responses

The contribution of the different ordering of TDMs describing the 'totality' of the 2DEV response within the $n = 3$ term of Eq. (2.60) can be written neatly in a set of nested commutators:

$$\mathbf{S}^{(3)}(\tau_3', \tau_2', \tau_1') = \left(\frac{i}{\hbar}\right)^3 \langle\langle\alpha|\,[[[\mu_{v4}, \mu_{v3}], \mu_{e2}], \mu_{e1}]\,|\alpha\rangle\rangle_E, \tag{2.61}$$

where the spot of each μ in the nested commutators is determined by the time ordering constraint; the number in the subscript determines that time ordering. Additionally, for clarity the subscript

'v' or 'e' is included to denote which TDMs correspond to electronic transitions and which to vibrational transitions. This notation is similar to that in Ref. [28] and can be implemented conveniently. Note that the commutators in Eq. (2.61) also capture on which side of the Feynman diagram the interactions occur.

As an illustration, the linear (electronic) response takes the form of

$$\mathbf{S}^{(1)}(\tau_1') = \left(\frac{i}{\hbar}\right) \langle\langle\alpha| \left[\mu_{e2}, \mu_{e1}\right] |\alpha\rangle\rangle_E, \tag{2.62}$$

which features one time interval and two TDM operators at each end of this time interval.

2.2.5 Feynman Diagrams

For a third order response, the $2^3 = 8$ unique *double sided Feynman diagrams* are shown in Fig. 2.2. Their 8 complex conjugates are not shown, but could be represented by the mirror images of these ones. They are categorised as being either 'Rephasing' or 'non-rephasing' diagrams[24]. Four types can be distinguished, as described in Fig. 2.2. Each diagram corresponds to a specific physical process.

From left to right are shown the ground state bleach (GSB), excited state absorption (ESA), excited state emission (ESE) and ground state emission (GSE) diagrams. Notably, the first letter in these diagram names reflects whether the IR interactions (the final two in each diagram) occur in the electronic ground or excited state. The sequence of TDM operators, seen in Eq. (2.61), is written underneath each diagram.

A priori, each of these processes can occur with the same probability. 2DEV spectra are therefore a reflection of the strength of these different Feynman diagrams: The strength is determined by the specific combinations of the TDMs and therefore depends on the system's nature.

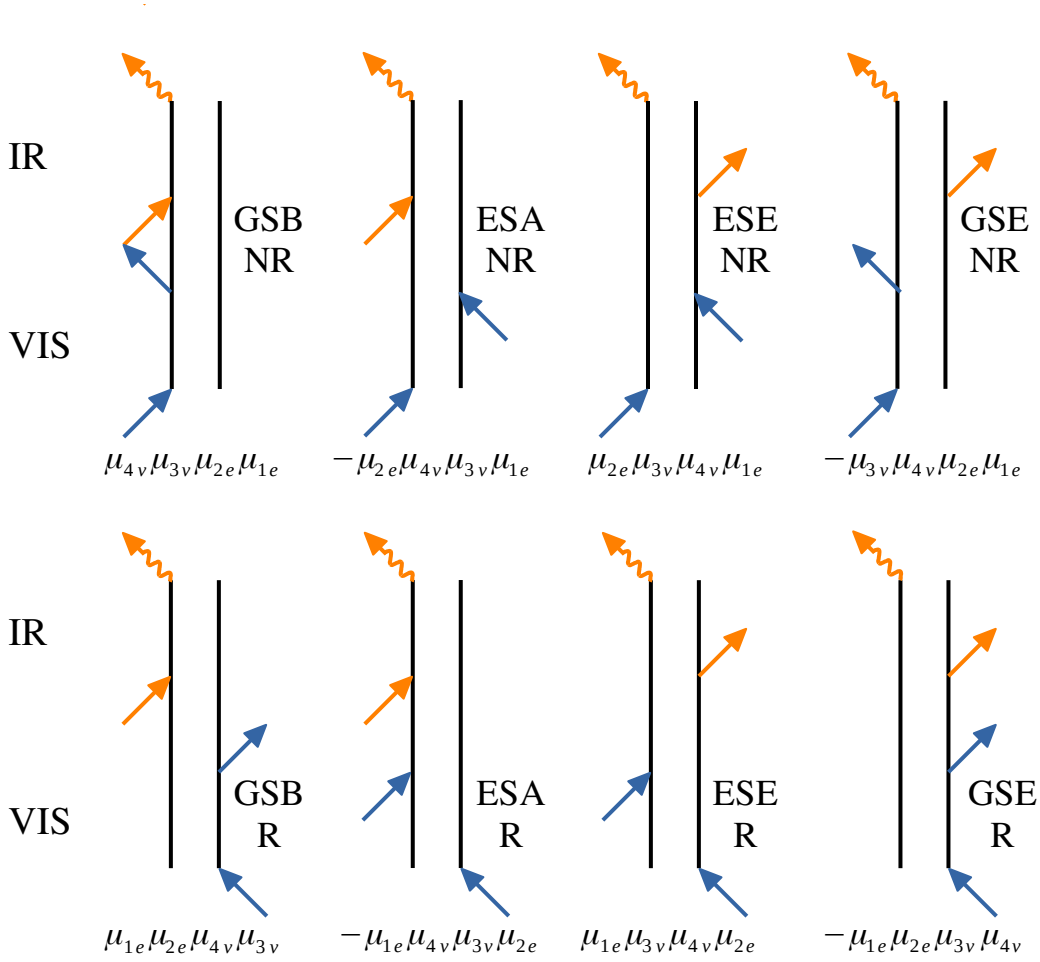

FIGURE 2.2: The different Feynman diagrams that are calculated in order to obtain the 2DEV spectra, Each diagram corresponds to a specific sequence of interactions with the external electromagnetic fields. The Top row displays the non-rephasing diagrams, while the bottom row displays the rephasing diagrams. From left to right are shown the ground state bleach (GSB), excited state absorption (ESA), excited state emission (ESE) and ground state emission (GSE) diagram types.

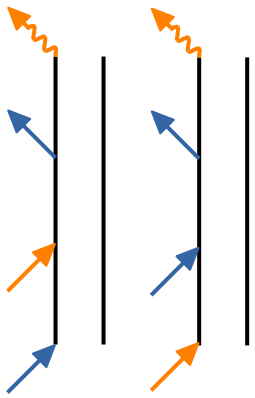

FIGURE 2.3: Two examples of Feynman diagrams that are not included in the calculations of this work. The main difference with those in Fig. 2.2 is that the order of infrared and visible pulses are exchanged in time. As is often done, this work assumes that the system's interactions with the external magnetic fields are instantaneous, i.e. the pulse envelopes are assumed to have delta function shape. Therefore, the interactions happen in the well defined order, depicted in Fig. 2.2.

2.2.6 Non-zero Temperature

In this work, the response to the system at non-zero temperature (used in the heterodimer analysis) is calculated as follows. The response R corresponding to a single pathway is calculated as

$$R = \langle\alpha|\,\mathbf{S}\,|\alpha\rangle\,, \tag{2.63}$$

where $|\alpha\rangle$ denotes a state in site basis and $\mathbf{S}$ denotes the product of constants, transition dipole and time evolution operators relevant for the investigated response type, e.g. linear or 2DEV. One can calculate the response R to a superposition of eigenstates labelled by A, weighted by a Boltzmann factor as

$$R = \sum_A \exp(-E_A/kT)\,\langle A|\,\mathbf{S}\,|A\rangle\,. \tag{2.64}$$

One can insert complete site basis sets, denoted by α and β in order to write the response as follows:

$$\begin{aligned} R &= \sum_{A,\alpha,\beta} \exp(-E_A/kT)\,\langle A|\alpha\rangle\,\langle\alpha|\,\mathbf{S}\,|\beta\rangle\,\langle\beta|A\rangle && (2.65)\\ &= \sum_{A,\alpha,\beta} \left(\exp(-E_A/kT)\,\langle A|\alpha\rangle\,\langle\beta|A\rangle\right)\langle\alpha|\,\mathbf{S}\,|\beta\rangle && (2.66)\\ &= \sum_{\alpha,\beta} \left(\sum_A \exp(-E_A/kT)\,\langle A|\alpha\rangle\,\langle\beta|A\rangle\right)\langle\alpha|\,\mathbf{S}\,|\beta\rangle && (2.67)\\ &= \sum_{\alpha,\beta} f_{\alpha\beta}\,\langle\alpha|\,\mathbf{S}\,|\beta\rangle\,. && (2.68) \end{aligned}$$

The result is an expression where the response function is calculated in terms of site states. Note that in this definition it need not be the case that the system's site Bra and Ket are identical. This could be relevant if both the two specific site states α and β contribute to eigenstate A. However, this does not occur for the states in the electronic ground manifold, since they are not mixed in the models considered in this work, but it does occur for states in the electronically excited manifold, relevant at higher temperatures.

The inner products $\langle A|\alpha\rangle$ and $\langle\beta|A\rangle$ are found in the matrix elements of U, which is defined by

$$H_{\text{eig}} = U^{-1} H_{\text{site}} U, \tag{2.69}$$

where the columns of U are the eigenvectors of H_{site}. The inner product $\langle A|\alpha\rangle$ is then found at column 'A' and row 'α', while $\langle A|\beta\rangle$ is the complex conjugate of the U element at the respective indices.

Calculating the factors $f_{\alpha\beta}$ requires negligible computational effort, while the terms $\langle\alpha|\,\mathbf{S}\,|\beta\rangle$ are expensive. For computational efficiency, it is chosen to reduce the number of terms in the final expression of Eq. (2.68). This is done by introducing a threshold: only include terms for which $|f_{\alpha\beta}| > \frac{1}{1000}\sum_{\alpha,\beta} f_{\alpha\beta}$. Doing this at a temperature of e.g. $kT = 10$ cm^{-1} yields a selection that is limited to α and β being the ground state.

2.2.7 External field polarisations

A molecule can have transition dipole moment components in all three different spatial directions due to its morphology. These TDMs couple to the electric component of the external electromagnetic fields. Hence the polarisation of the different pulses with which a molecule interacts impacts the molecule's response. Therefore, an ensemble of molecules will also respond differently to different external fields' polarisation directions. It is considered here that the ensemble of molecules is isotropic on the scale of the ensemble.

In the case of linear absorption, if the molecules do not rotate between the two interactions with external field, then 'ingoing' and 'outgoing' electromagnetic waves will be polarised in the same direction. Hence the response will be proportional to the inner product of the TDMs at the two respective interaction times $R \propto \sum_{i,j} \left\langle \mu_i^{(1)} \mu_j^{(2)} \right\rangle_E = \left\langle \mu_x^2 + \mu_y^2 + \mu_z^2 \right\rangle_E$, where the sum i, j is over the three spatial directions, the subscript E denotes the ensemble average and the superscripts denote the time ordering. Because of the symmetry of a vector product, naturally no prefactor is added to any of the three terms.

Similarly for a 2D response, the response in general form is proportional to

$$R \propto \sum_{i,j,k,l} f_{i,j,k,l} \left\langle \mu_i^{(1)} \mu_j^{(2)} \mu_k^{(3)} \mu_l^{(4)} \right\rangle_E, \tag{2.70}$$

where the subscripts denote the spatial directions ($\in [x, y, z]$) and the superscripts denote the TDM ordering corresponding to the investigated Feynman diagram. This expression contains $3^4 = 81$ different geometrical terms (for each of the Feynman diagrams) and these do get a prefactor $f_{i,j,k,l}$. All different orientations of the individual molecules are considered and the relative probability for the molecules' TDM components to match the direction of the external field polarisations is what goes into these prefactors.

In this work we consider dimers that feature cylindrical symmetry. Hence a molecular frame of reference may be chosen such that the z-component of the molecules' vibrational and electronic TDMs are zero. This means that in Eq. (2.70) only the x and y components need be considered. This yields $2^4 = 16$ different geometrical terms. Because of the ensemble isotropy, terms with a single 'x' or 'y' such as $\mu_x\mu_y\mu_x\mu_x$ do not contribute. As a result, only eight different geometrical terms remain to be calculated.

Two different polarisation setups are discussed here: 'parallel' and 'perpendicular'. These have external field polarisations of 'xxxx' and 'xxyy' respectively. The prefactors in Eq. (2.70) are different for these two setups, which results in different 2DEV spectra, depending on the investigated molecules' nature. Most notably, the largest contributing terms $\mu_x\mu_x\mu_x\mu_x$ and $\mu_y\mu_y\mu_y\mu_y$ get a prefactor three times lower in the perpendicular compared to the parallel setup. See Ref. [30] for further details. In conclusion, these geometrical considerations thus lead to calculating eight geometrically different 2DEV responses for each polarisation setup.

Chapter 3

Numerical Methods

3.1 Main numerical procedure

The method of calculating 2DEV spectra for the described dimer systems in the previous sections is too involved to attempt doing analytically and must therefore be implemented numerically. A flowchart of this process is shown in Fig. 3.1, where the main procedures are described.

The core of the computational method is Numerically integrating the Schrödinger equation (NISE), which is the procedure used to determine the system's time evolution [31]. It's basic assumption is that over a small time interval, the system's Hamiltonian does not change, which allows for easy incremental integration of the Schrödinger equation and hence the determination of the time evolution operators.

The interaction potential is considered a perturbation in the derivation reproduced in the previous chapter and perturbation theory is applied to this time-dependent aspect of the 2DEV investigation: the interactions with the electromagnetic field. However, the fluctuations in the system's Hamiltonian due to bath coupling are treated in a more straightforward manner. The time dependent fluctuations are calculated via the expression in Eq. (2.39) for each increment in time Δt_i, where the subscript i denotes which of the time domains is considered (t_1, t_2 or t_3). The Hamiltonian is assumed to be constant over each of the time steps (with length Δt_i). The time evolution is then simply calculated by $U(t_i + \Delta t_i, t_i) = \exp\left(-\frac{i}{\hbar} H(t_i)\Delta t_i\right)$ [26].

The procedure for calculating a 2DEV spectrum for a single dimer trajectory (a single bath realisation) is as follows. The 2DEV response is ultimately calculated on a 2D time loop over t_1 and t_3. The aim is to do as much work as possible outside of this double loop. Before the double loop is started,

1. establish which temperature terms are included, by selecting the initial states that pass the threshold defined in section 2.2.6 or manual selection.

2. generate the random trajectories for each of the fluctuating Hamiltonian entries,

3. do as much work as yet possible on the interaction picture transition dipole operators, by calculating the time evolution operators for the three time intervals. That requires generating the Hamiltonians on each time point on the three time intervals. The t_2 interval is assumed to have the same time resolution as the t_3 interval. The first TDM $\mu_{1e}(0)$ is finalised outside the double loop and some pre-work can be done on the other three TDMs in order to avoid doing it redundantly.

Inside the double t_1, t_3 loop the following is done:

4. Finalise the transition dipole moment operators by multiplying the generated TDMs in Schrödinger picture with the appropriate time evolution operators.

5. So far, the TDMs are known for each of the two dimer molecules for each interaction. Now for each of the four interactions with the electromagnetic field, determine the total system TDMs in the three geometrical directions. This allows for calculating the external fields polarisation dependence.

6. Calculate the 2DEV Feynman diagrams by multiplying the different TDMs in all different orderings mentioned in section 2.2.5 and taking the inner products with the initial system state. This is done for each of the eight geometrical terms mentioned in section 2.2.7.

7. These different terms are given different geometrical factors and then added up to form the 2DEV response at one point on the 2D time grid, for a single bath trajectory.

Once the 2D time loop is completed, the 2DEV response in time domain is found for a single realisation. The above procedure is then repeated for $N = 1000$ realisations in case of the homodimer.

Once the ensemble average 2DEV response is calculated, the frequency response domain (spectrum) is calculated by 2D Fourier transform of the response corresponding to each each Feynman diagram. As mentioned in section 2.2.5, there are two classes of diagrams: rephasing and non-rephasing, R and NR. The 2D response contains both 'absorptive' and 'dispersive' components which have different lineshapes: the dispersive components feature 'phase twists' [24] that cause broadening and part of the lineshapes' region to be positive and another part to be negative. These R and NR diagrams occur in different quadrants of the Fourier Plane and can be combined in order to cancel the dispersive components to the signal by summing them while inverting the t_1 axis of the R diagrams, as in

$$R_{abs}(\omega_1, \omega_3) = R_R(-\omega_1, \omega_3) + R_{NR}(\omega_1, \omega_3), \tag{3.1}$$

which is based on the expression in Ref. [24]. The result is a so called 'absorptive' 2D spectrum, the characteristic feature of which is that its lineshapes are more narrow and are symmetric and hence more easily interpretable than the separate R and NR spectra.

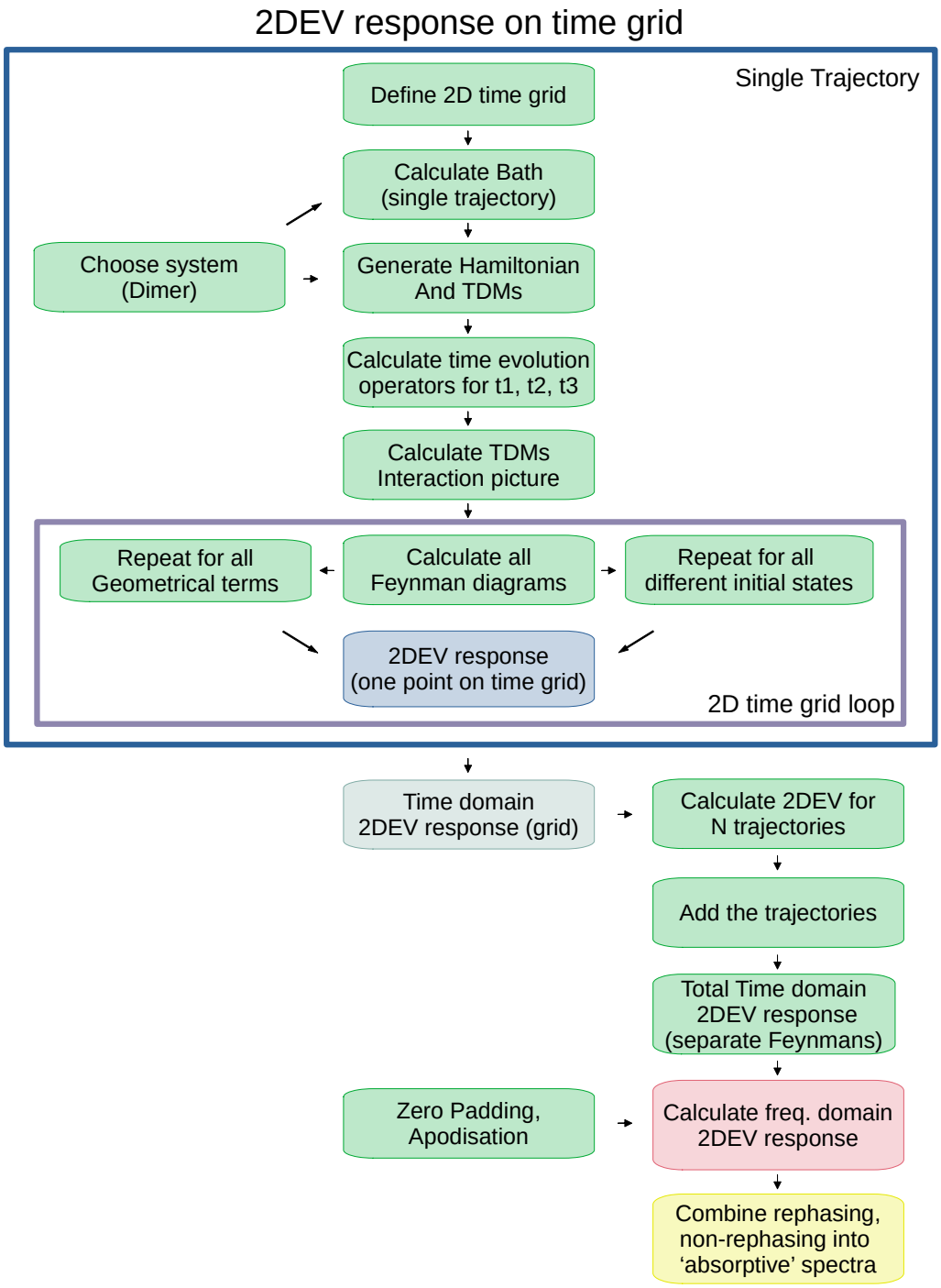

FIGURE 3.1: A flowchart illustrating the implementation of the main 2DEV calculations done in this work. The main steps are shown, not specific tricks used to make the computation feasible or specific ways of organising the code. A few key points in the method are the Hamiltonian generation for each fluctuation in each bath trajectory, the calculation of the transition dipole moments in interaction picture, the calculation of the 2DEV response function at each point on the 2D time grid, the summing of all realisations, the zero padding and the final Fourier transform to frequency domain.

Note that the dimer Hamiltonian is block diagonal in the sense that the electronic ground and excited blocks are uncoupled. That allows for the time evolution to be treated separately for each block, which saves computational power, because matrix multiplication goes as N^3. Moreover, Hamiltonian diagonalisation, used in calculating the matrix exponentials of the Hamiltonians on each time point is also done more efficiently for two smaller matrix blocks than for the complete matrix.

Hence U_{gg} and U_{ee} are calculated for the ground and excited manifold respectively. In line with this, the electronic TDMs are separated in μ_e^{eg} and μ_e^{ge}, allowing for the transition between the manifolds. Moreover, the vibrational TDMs are also block diagonal and can therefore be separated in μ_v^{gg} and μ_g^{ee}, since they treat transitions within each respective manifold.

Another thing worth noting is that the TDMs are generated separately for the different sites, which allows for the introduction of an angle between them. In the code used in this work, the time evolution is done separately for the different site TDMs and the TDMs are later combined via a *dimer angle*, but in retrospect it would be slightly faster to calculate the combine the different site TDMs first and do the time evolution later.

The fact that the ground and excited manifold matrix blocks are uncoupled means that one can shift the energy difference between these blocks, the exciton energy, to zero, or near zero in case of an excitonic gap. The vibrational modes retain their original frequencies. Making this shift means that the electronic frequencies relevant to the system are much lower (near zero), which means that a lower time resolution is needed for an accurate time evolution computation. Equivalently, making this shift allows for a more efficient use of the chosen time grid. After the Fourier transform, the frequency axis can be shifted back to the physical values. In line with the works [6, 22] that inspired these investigations, the shift back to physical values is *not* done for the heterodimer discussed in section 4.1, but *is* done for the homodimer in section 4.2 with an exciton energy of 18190 cm^{-1}.

3.2 Further considerations on computational tractability

The multidimensional spectra calculations can get expensive quite quickly if one is not careful. Factors that directly impact the computational cost, along with ways to tackle them are:

- System (Hamiltonian) size: having a larger basis set describing the phenomena in the system allows for 'richer' physics to be probed, but is expensive.
  - Tackle: choose the smallest basis set needed to probe the investigated phenomena. 1) The system only interacts twice with an EM pulse that could change the electronic state (the first two pulses, see Fig. 2.2. Moreover, on either site of the Feynman diagram, the initial state on either side must be in the same electronic manifold. Hence only two

different electronic states need be included: a double electronically excited state is not relevant in 2DEV spectroscopy that probes a system starting in the ground manifold. 2) The same is the case for the on-resonance vibrational mode: 2DEV spectra on a system with *small vibronic coupling* (either HT or FC) in that mode will mainly require a single vibrational excitation therein, for the same reason: double vibrational excitation will 'not' be reached in the on-resonance mode. 3) For other vibrational modes, choose a number of vibrational states that is appropriate for the vibronic coupling strength: more states if the coupling is stronger.

In the homodimer, a maximum of 8 vibrational states are allowed in the system, spread over either site, giving a total Hamiltonian size of 135. (The vibrational frequency is the same for both sites and for both ground and excited manifold, which allows for simple truncation by counting the total vibrational quanta present in the system.) In the heterodimer, up to a single electronic excitation, up to a single on-resonance mode quantum and up to three off-resonance mode quanta are allowed, yielding a Hamiltonian size of 36.

- Number of 'temperature terms': this means the number of states that are in the initial superposition and in thermal equilibrium.
  - Tackle: include those states that correspond to significant 2DEV spectra contributions. This means eigenstates that have sufficient initial population (via Boltzmann factor) and overlap with the relevant states in site basis, as described in section 2.2.6. The homodimer investigated in this work is assumed to start in absolute ground state, while the heterodimer (at $kT = 105$ cm^{-1}) starts in a superposition of all states in the off-resonance mode in ground manifold.
- Number of realisations (different dimer trajectories): calculating the ensemble average 2DEV response requires computing the response for a large number of different bath trajectories. The larger the bath fluctuations, the more realisations need be included in order for the response to converge to the ensemble average.
  - Tackle: find the number of realisations beyond which the response function barely changes by visual inspection of the 2DEV spectra. 1000 realisations were found to be appropriate for the homodimer investigated in this work. It was found useful to compute the random trajectories in parallel, giving each a unique seed.
- Size of time grid: large enough to probe the essential physics. Most of the interesting fluctuations of the time response for either of the time domains involved in multidimensional spectra happen in the beginning of the time interval: the functions are 'decaying oscillations'. Hence after a certain time, depending on the system itself and the bath coupling, the response

function is effectively noise. Probing that noise is unnecessary, yet one might still want to have a long time sample in order to obtain a high resolution in the 2DEV spectra.

- Tackle: sample the 2DEV response function up to the time when the response has effectively fully 'decayed', for both t_1 and t_3. Apply zero-padding to this response, which means adding the 'zero signal' at the end of the sampled signal in order to obtain a response function signal as if it were sampled for a long time. Since it is known that the function will decay to zero after sufficient time anyway, no 'unphysical' data is fabricated here.

  However, this zero-padding can introduce artefacts in the Fourier transformed 2DEV spectra if the sampled response has not sufficiently decayed at the end of the sampling interval. In that case the response in time domain can be described as convoluted with a step function, the Fourier transform of which is a sinc function. Hence an artefact that can be introduced by zero padding is the convolution of the 2DEV spectra with sinc functions in either/both ω_1 or ω_3 direction, depending on whether there has been sufficiently long sampling in the respective time domains.

  A way to deal with this artefact is to multiply the time response signals with apodisation functions, such as a decaying exponential $\propto \exp(-t_i/\Lambda_i)$ and/or a Gaussian $\propto \exp(-(t_i/\sqrt{2}\sigma_i)^2)$. This can smoothen the 'step' to the padded zeros and reduce the artefact. Moreover, this apodisation makes the calculated spectra 'smoother'.

All in all, it is a bit of an art to play around with the grid size, basis truncation, number of realisations, apodisation functions etcetera in order to get a decent 2DEV spectrum within a reasonable time frame. Hence, certain calculation parameters are established relatively arbitrarily by checking at which 'accuracy' the calculation converges sufficiently well. The parameters chosen for the hetero- and homodimer calculations are given in Appendix A and B respectively.

Chapter 4

Results

In this chapter, the methods outlined in the previous chapter are used in order to answer the three main goals of this work, as described in the introduction: 1) reproduce the basic 2DEV results in a previous theoretical work on the heterodimer [6], which will be 2DEV spectra for three different vibronic coupling cases, 2) expand on those results, which is done by varying the angle between the transition dipoles for the chromophores and 3) calculate 2DEV spectra for a homodimer that has not yet been investigated with 2DEV [22]. The heterodimer is discussed first.

4.1 Heterodimer

The first thing that we will try to reproduce is the basic 2DEV spectrum calculated for three vibronic cases investigated in Ref. [6]. Those three 2DEV spectra are copied here in Fig. 4.1 for convenience of the reader. The main conclusion of this comparison is that the different vibronic coupling cases leave slightly different trace in the 2DEV spectra, most notably in the 'high frequency' region around 400-500 cm^{-1} on the electronic axis. The details of the different peak origins, positions and colours in the figure will be discussed later on in this section. For now these spectra are shown to give the reader an impression of what will be tried to calculate.

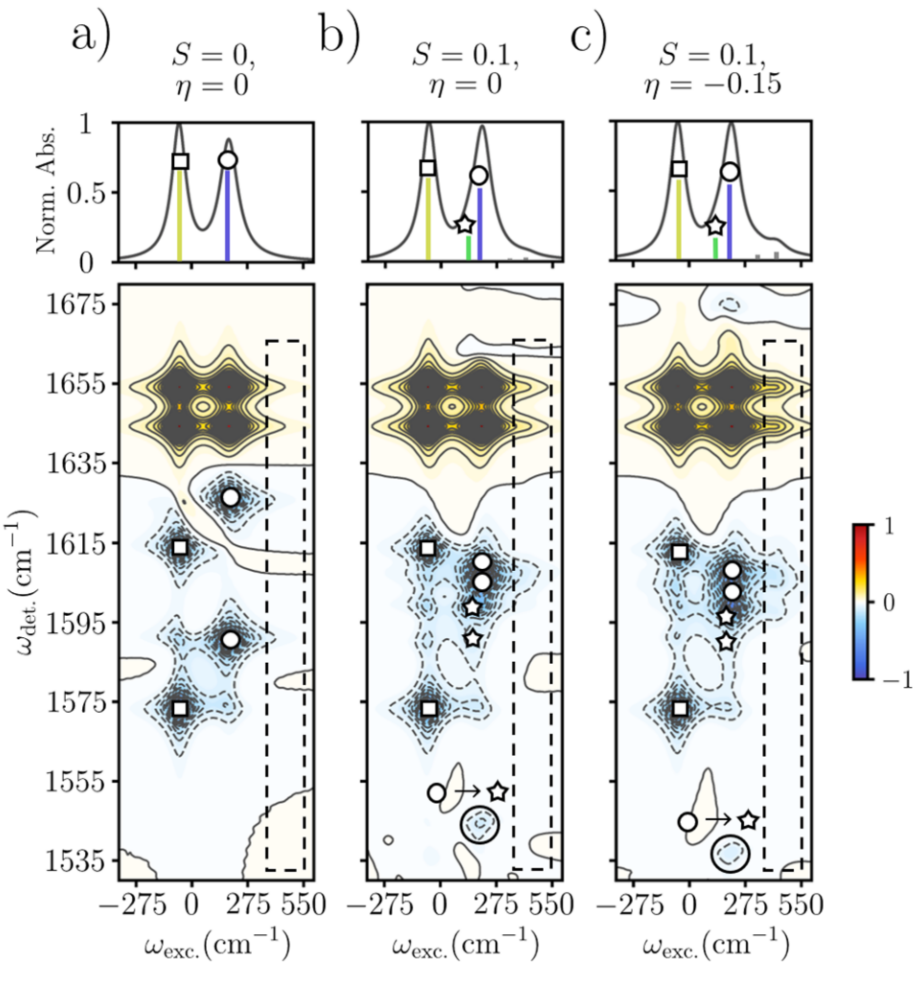

[H]

FIGURE 4.1: The basic 2DEV calculation at waiting time (t_2) zero for three vibronic cases in the heterodimer published in Ref. [6] and copied here. Each column in the figure represents a different vibronic coupling configurations, characterised by the two parameters S and η written above, which represent the strengths of the Franck-Condon and Herzberg-Teller activities in the off-resonance vibrational mode respectively. Hence the left column represents a system with no vibronic activity in the off-resonance mode, the middle has FC activity, and the right one has both FC and HT. The top row shows the linear absorption spectra for the three different cases. See the original work for more details. The bottom row shows the corresponding 2DEV spectra. The horizontal axis corresponds to the electronic 'E' part of the 2DEV, the first part of the Feynman diagrams. The vertical axis corresponds to the infrared 'V' part of the 2DEV, the second part of the Feynman diagrams. The linear absorption frequency band matches the electronic band on the horizontal axis of the 2DEV spectra and have identical ranges.

4.1.1 Reproduction of basic 2DEV result

In Fig. 4.2 the first attempt at reproducing the simplest vibronic case (leftmost column in Fig. 4.1 is shown and is compared with the simplest vibronic case result calculated in Ref. [6]. The

linear spectrum shows two main peaks: one electronic peak 'corresponding' to each site. They have their main origin in the electronic part of the Hamiltonian, Eq. (2.6): the excitonic gap (100 cm^{-1}) combined with the dipole-dipole coupling (also 100 cm^{-1}), which means that these peaks are found at approximately $\omega_{vis} = (\Delta E \pm \sqrt{\Delta E^2 + 4 * J^2}/2$, which are ~ -62 and ~ 162 cm^{-1}. In addition, there are slight shifts due to the vibronic coupling in the on-resonance mode, which is 'on' with $S_f = 0.005$ for all three vibronic cases. Extra peaks at higher frequencies occur when there is non-zero vibronic activity in the off-resonance mode. The 2DEV spectra show the same division into two main 'columns' of peaks on the electronic axis, matching the two main absorption peaks in the linear absorption.

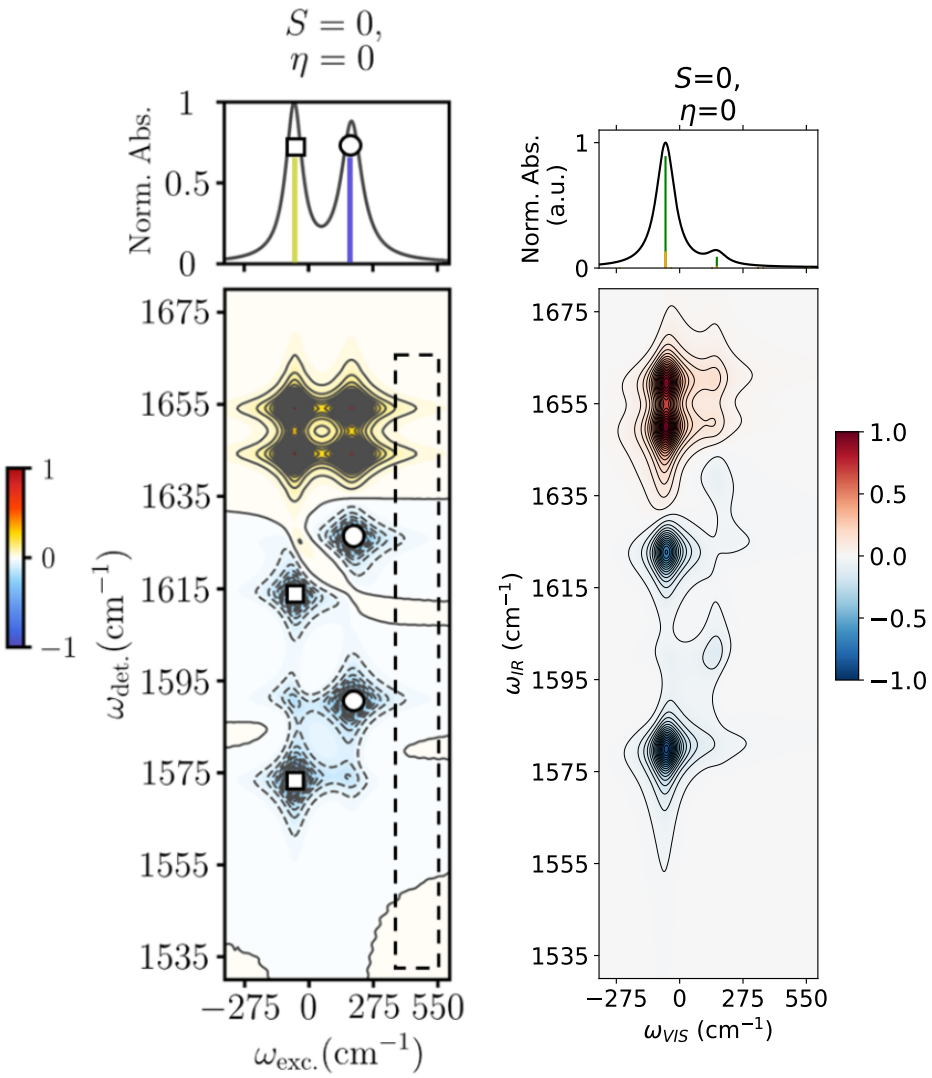

FIGURE 4.2: The initial attempt at the reproduction of the 2DEV spectrum for the simplest vibronic case calculated in Ref. [6]. The leftmost column in Fig. 4.1 is cut out for easy comparison and is shown here on the left: this is the original work in Ref. [6]. The right 2DEV and absorption spectra in this figure are calculated in this work. The specifics of the calculation are presented in Appendix A and an effort is made to set the plot parameters such that easy comparison is possible. The vertical lines in the linear absorptions are stick spectra to illustrate which lines contribute. In the right (new) linear spectrum, the colours of the sticks denote the different initial state contributions (and hence reflect the non-zero temperature effects). Many contour lines are plotted to match the style of the original work and to demonstrate less prominent 2DEV features. Zoom in on the PDF for better visibility (vector graphics).

Without yet trying to analyse every feature in either 2DEV spectra, one prominent difference can immediately be seen between the original work and the first attempt here. In the new calculation, the right peak in the absorption spectrum is much lower than the left; the same holds for the right column of peaks in the 2DEV spectrum. This is not the case in the original calculation

in Ref. [6], shown in Fig. 4.1, where the two main absorption peaks are approximately the same in height. This difference is also observed for the two other vibronic cases, shown in the 2DEV spectra added in Appendix C.

In the new calculation, the peak height differs by a factor ~ 10. Since this ratio is found for all three vibronic cases and in both the absorption and 2DEV spectra, it can be deduced that this difference is rooted in the 'electronic' parameters of the calculation. That means that the coupling J, the electronic transition dipole moment ratio μ_A/μ_B and the excitonic gap ΔE are involved. (All the vibrational parameters play a much smaller role in this peak ratio.) That is, if the calculation is qualitatively done 'correctly'.

After checking (and correcting!) the computer code many times, it was decided to investigate whether the parameters presented in Ref. [6] were indeed the ones used. A simple model Hamiltonian, mimicking the electronic part of the heterodimer was set up, with varying excitonic coupling and varying electronic TDM ratio's. The excitonic gap was assumed correct (100 cm^{-1}), given the matching peak location in the absorption spectra. The ratio of the 'left' and 'right' absorption peaks was calculated for varying μ_A/μ_B and J. The result is shown in Fig. 4.3 and a qualitative discussion of the figure's main features is provided.

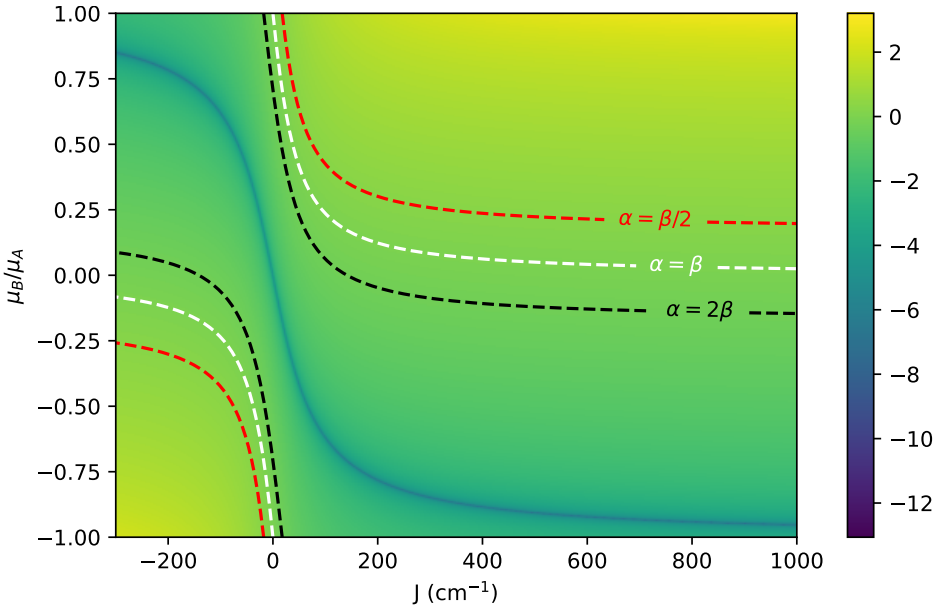

FIGURE 4.3: Shown is $\log_{10}(I_\beta/I_\alpha)$, the log ratio of the two 'exciton' peak heights in linear absorption of a simple three state Dimer system as function of the site TDM ratio μ_B/μ_A and exciton coupling J. Zero temperature is assumed. Note that A and B denote the sites (site basis) while α and β denote the two 'excitonic' eigenstates. The excitonic gap in this dimer is $\Delta E = 100$ cm^{-1}. In those dimers considered in this work that include one or more vibrational modes, the ratio of the two main 'exciton' peaks is primarily determined by the dipole-dipole coupling J and by the ratio of the oscillator strengths: μ_B/μ_A. That is, if the vibronic coupling is 'small', i.e. when the Frank-Condon and Herzberg-Teller coupling are small. A slice of this figure at $\mu_B/\mu_A = 1/4$ can be seen in Appendix D.
The fine blue line indicates the region in parameter space where one of the two eigenstates is dark: the 'right' peak corresponding to 'site B' has zero intensity on the blue line parameter region. The three dashed lines indicate the regions where the linear absorption peaks have the indicated ratios. Note that the peaks are equal in height for zero coupling J with a TDM ratio of one (two identical, uncoupled sites). Moreover, the figure shows a symmetry: the peak ratio is invariant when both the TDM ratio μ_B/μ_A and J are inverted.
Another peculiar observation is that two peaks of non-zero height exist in a dimer that has a TDM of zero at one of the sites. This happens at the line of $\mu_B/\mu_A = 0$ if the coupling J is non-zero: due to the coupling, 'site B' borrows oscillator strength from 'site A'.

It is found that at the published parameters ($J = 100$ and $\mu_A/\mu_B = -1/4$), the absorption peak ratio is indeed $I_\alpha/I_\beta \sim 10$, as found in the new 2DEV calculation shown in the right column of Fig. 4.2. From Fig. 4.3, it was expected that either the dipole strength ratio μ_A/μ_B or the excitonic coupling J used in the calculation of [6] was not as reported, but differed by a minus sign. When flipping the coupling to $J = -100$ cm^{-1}, the spectra shown in Fig. 4.4 are found, which

show a ratio of the left and right linear absorption peaks that is now closer to unity, approaching the spectra reported in Fig. 4.1, though slight differences still exist in the linear absorption. The minus sign flip in the original paper [6] was indeed confirmed by the first author Eric A. Arsenault.

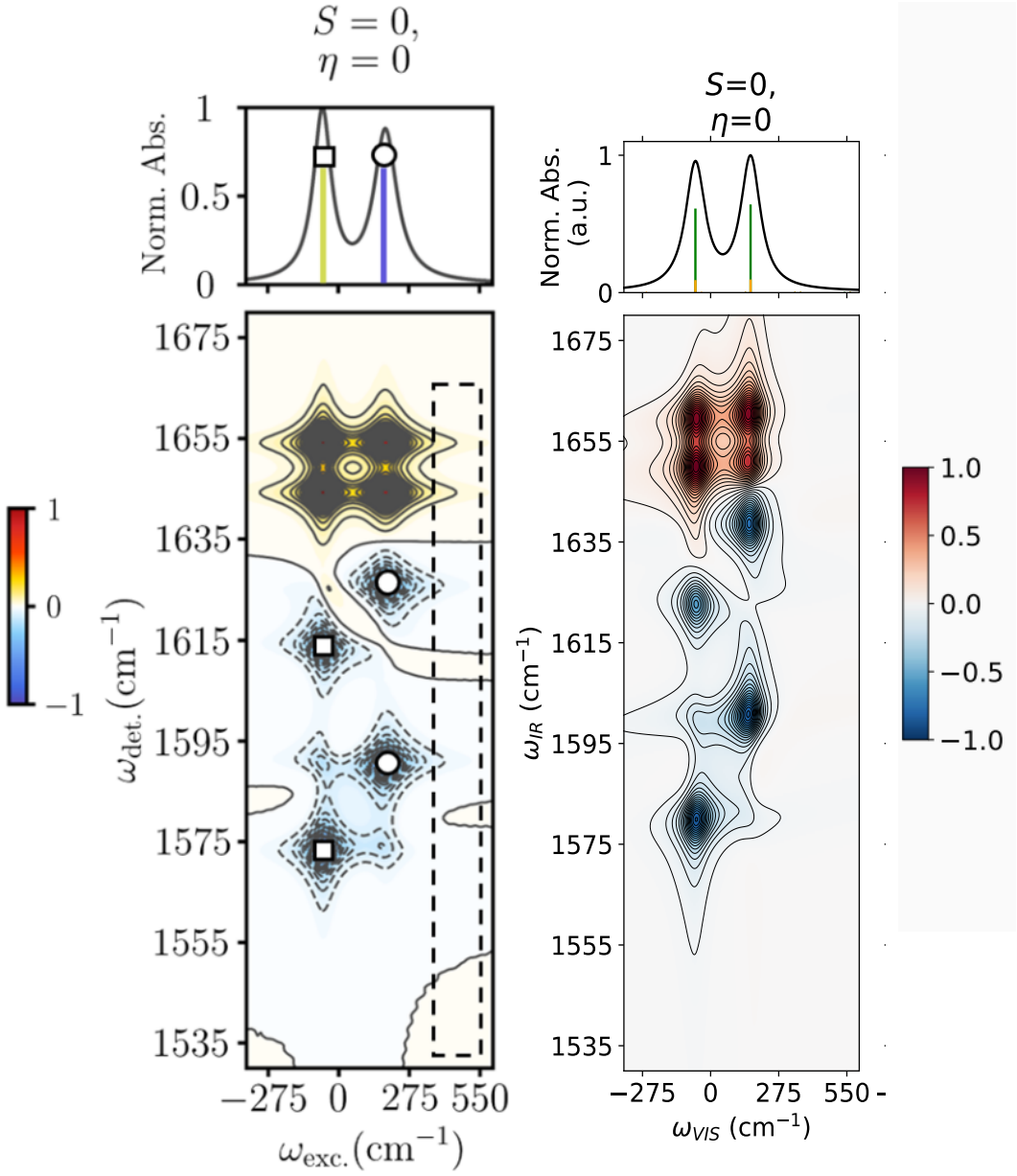

FIGURE 4.4: The second attempt at the reproduction of the 2DEV spectrum for the simplest vibronic case calculated in Ref. [6] (the leftmost column in Fig. 4.1). This time with $J = -100$ cm^{-1}. Other specifics of the calculation are reported in Appendix A

2DEV peak origins

Besides the clear distinction of two main columns in the 2DEV spectra due to the exciton peak coupling, other 2DEV features can also be understood. It is worth noting that in this simplest

vibronic case $S = 0$ and $\eta = 0$, which means that both FC and HT coupling, which are implemented in the off-resonance mode, are turned off. Four main peaks (near $\omega_{IR} \sim 1650$ cm^{-1}) are red, while four other main peaks and (two in either column) and additional smaller peaks are blue. In this case, the different colours correspond to different Feynman diagrams, as the diagrams have different sign, as described in section 2.2.5.

The four red peaks are 'ground state bleach' (GSB) signals in a square configuration: two columns for reasons described above and two rows because the two different sites have different vibrational modes. The high frequency (on-resonance) modes have frequencies of 1650 and 1660 cm^{-1} in the electronic ground states of site A and B respectively. In the ground state bleach process the system is 1) electronically excited and subsequently de-excited back to ground state and 2) vibrationally excited and subsequently de-excited. Moreover, the states in the electronic ground manifold are uncoupled to other states. Therefore the energy difference between the absolute ground state and the on-resonance vibrationally excited states on either site are also 1650 and 1660 cm^{-1}. The GSB peaks are expected to lie on exactly those values on the IR axis, which is exactly what is seen in the calculation of this work, the right 2DEV of Fig. 4.4.

The highest four blue peaks are ESA and are all a vibrational excitation and subsequent de-excitation in the electronically excited manifold. Each column corresponds to either site 'A' or 'B' being excited. In each column there are two blue peaks: the highest frequency blue peak (at 1630 or 1615 cm^{-1} in the left 2DEV of Fig. 4.4 corresponds to the vibrational excitation occurring in the electronic ground state on the site where the electronic excitation is *not*. The low frequency blue peak in each column(at 1573 or 1590 cm^{-1} in the left 2DEV of Fig. 4.4) corresponds to the pathway where vibrational excitation occurs on the same site as the electronic excitation.

There are also two ESA peaks of much lower intensity, one per column (at 1573 or 1590 cm^{-1} in the left 2DEV of Fig. 4.4). These two peaks occur at the same IR frequency as the aforementioned two ESA peaks. Their pathway is attributed to the vibrational excitation occurring in 'the vibrational mode' in the electronically excited state on the site where the electronic excitation is *not*. Yet, this 'excitation' is possible due to the dipole-dipole coupling between the sites.

Now all six peaks seen in both 2DEV's in Fig. 4.4 have a pathway attributed to them in terms of the 'site basis states'. These descriptions are not exact since the attributed 'site states' are not eigenstates, but the system is simple enough for some sense to be made out of these 'site state pathways'. It is not so simple for the homodimer in the next section.

The original calculation in the left 2DEV of Fig. 4.4 shows the GSB and ESA peaks at slightly different value: all at approximately 5 cm^{-1} lower frequency on the IR axis. Eric A. Arsenault was asked about the origin of this discrepancy and he attributed it to the system-bath implementation. In Ref. [6], the bath is implemented as a set of harmonic oscillators coupled to each energy level in the system Hamiltonian. In this work's presented 2DEV calculation of the

heterodimer however, the bath is not implemented: a proper ensemble average is calculated for the homodimer, but not for the heterodimer.

However, a few variations on baths were newly investigated, by letting all the vibrational modes' energies and exciton energies fluctuate with values such that the peak widths in Fig. 4.1 were approximately recovered. These investigations however, did not yield a shift in the peaks on the IR axis in the 2DEV spectra. One case is given in Appendix E. Indeed it can be understood that fluctuations on the ground manifold vibrational modes' energies yields a peak broadening, but no peak shift on the IR-axis, because the fluctuating states are uncoupled. Hence this work's bath implementation style cannot cause the 'extra 5 cm^{-1}' shift seen in Fig. 4.1. Further details on the original work's bath implementation are found in Ref. [6].

Three vibronic coupling cases

Using the updated model parameters used in Fig. 4.4, all three vibronic cases are calculated and shown in Fig. 4.5. Several observations can be made:

- The GSB peaks remain almost identical for the three cases, as in the original comparison in Fig. 4.1.
- The two main ESA peaks in the left column remain approximately in place for the three cases, which is also the case in Fig. 4.1.
- There is extra activity in the 400-500 cm^{-1} region on the electronic axis when FC or HT activity is turned on, though this is not seen as prominently as in Fig. 4.1.
- A feature emerges near $\omega_{IR} \approx 1550$ cm^{-1} when vibronic activity is turned on and it is slightly lower in frequency for HT than for FC, as in 4.1.
- Specific peak height ratios between the two columns do not exactly match those in Fig. 4.1, seen in the linear absorption spectra: in the new calculation, the right column is slightly higher than the left, in all three cases. This is not the case in the original three cases, where they are equally high or the left one is slightly higher. Still, the two main peaks are approximately equally high in all three cases.

Hence there is quite some similarity between the calculation of this work and that in Ref. [6]. The main remaining difference is the aforementioned 5 cm^{-1} shift on the IR axis.

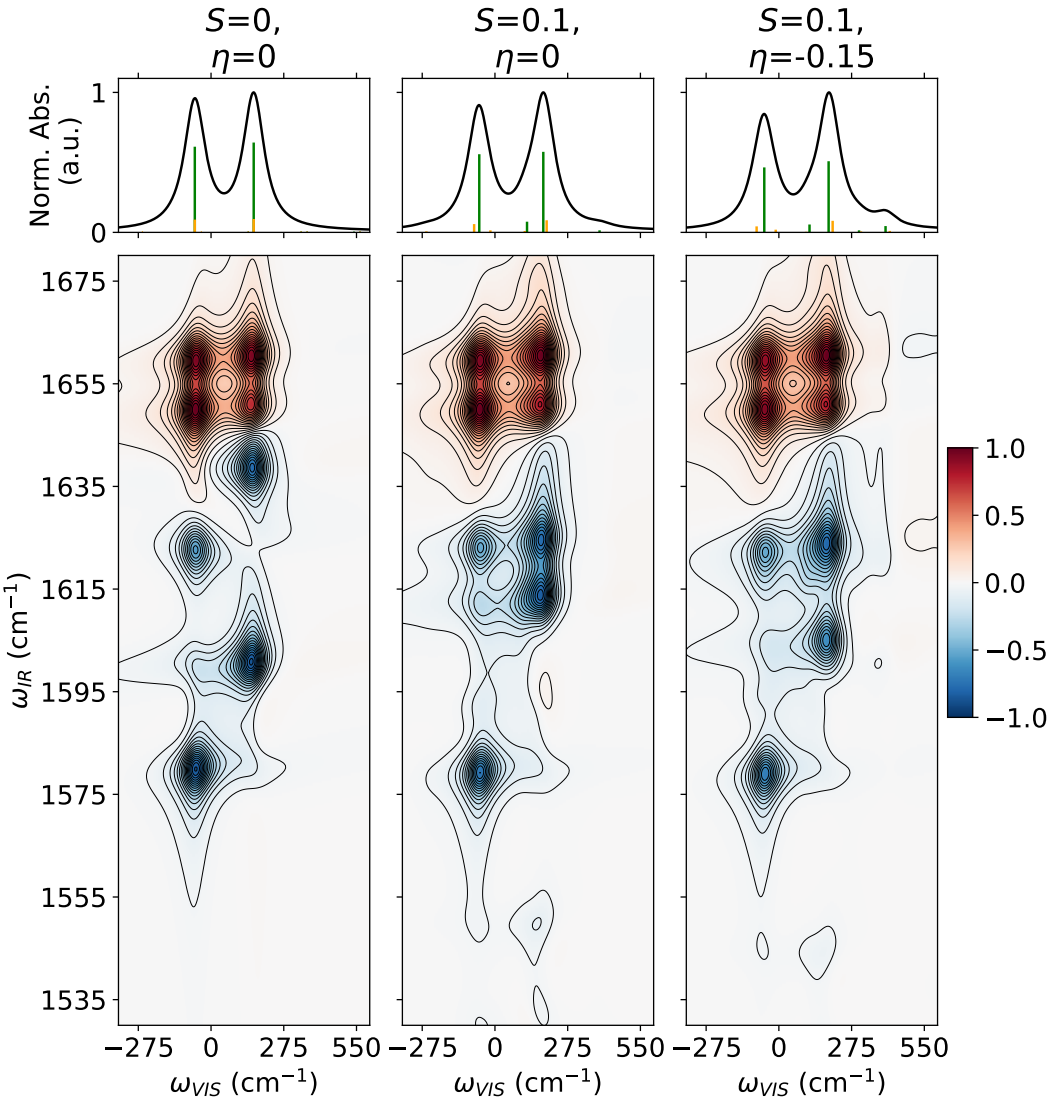

FIGURE 4.5: The 2DEV spectra for the same three vibronic cases discussed in Ref. [6], seen in 4.1.

ESE and GSE diagrams

Shown so far are the GSB and ESA Feynman diagrams. The ESE and GSE spectra that are described in Fig. 2.2 do not seem to yield more information compared to the GSB and ESA spectra and are effectively a mirror image of Fig. 4.5. For completeness, the ESE and GSE diagrams are shown in Fig. 4.6. These peaks are found at the same position on the visible axis, but at the inverted positions on the infrared axis, which can be understood from the diagrams in Fig. 2.2. In the second stage (t_3 interval) of the Feynman diagrams, for ESA and GSB the third interaction (which is an infrared pulse) happens on the left side of the diagram, while for ESE and GSE this interaction happens on the right side of the diagram.

The vibrational mode that is on resonance with this pulse only has two levels in this system, with a very low (0.005) Huang-Rhys factor. That in turn means that during the t_3 interval the high mode excitation sits on the Bra side for GSE and ESE and on the Ket side for GSB and ESA. It is precisely the difference of energy between the two sides of the diagram during a time interval that determines a peak's frequency corresponding to that time interval. The relevant expression for the 2DEV spectra's peak position is the relevant time evolution element $\propto \exp(-i/\hbar * (E_{Bra} - E_{Ket})t_3)$, explaining the position of GSE and ESE peaks in different quadrants of the Fourier plane.

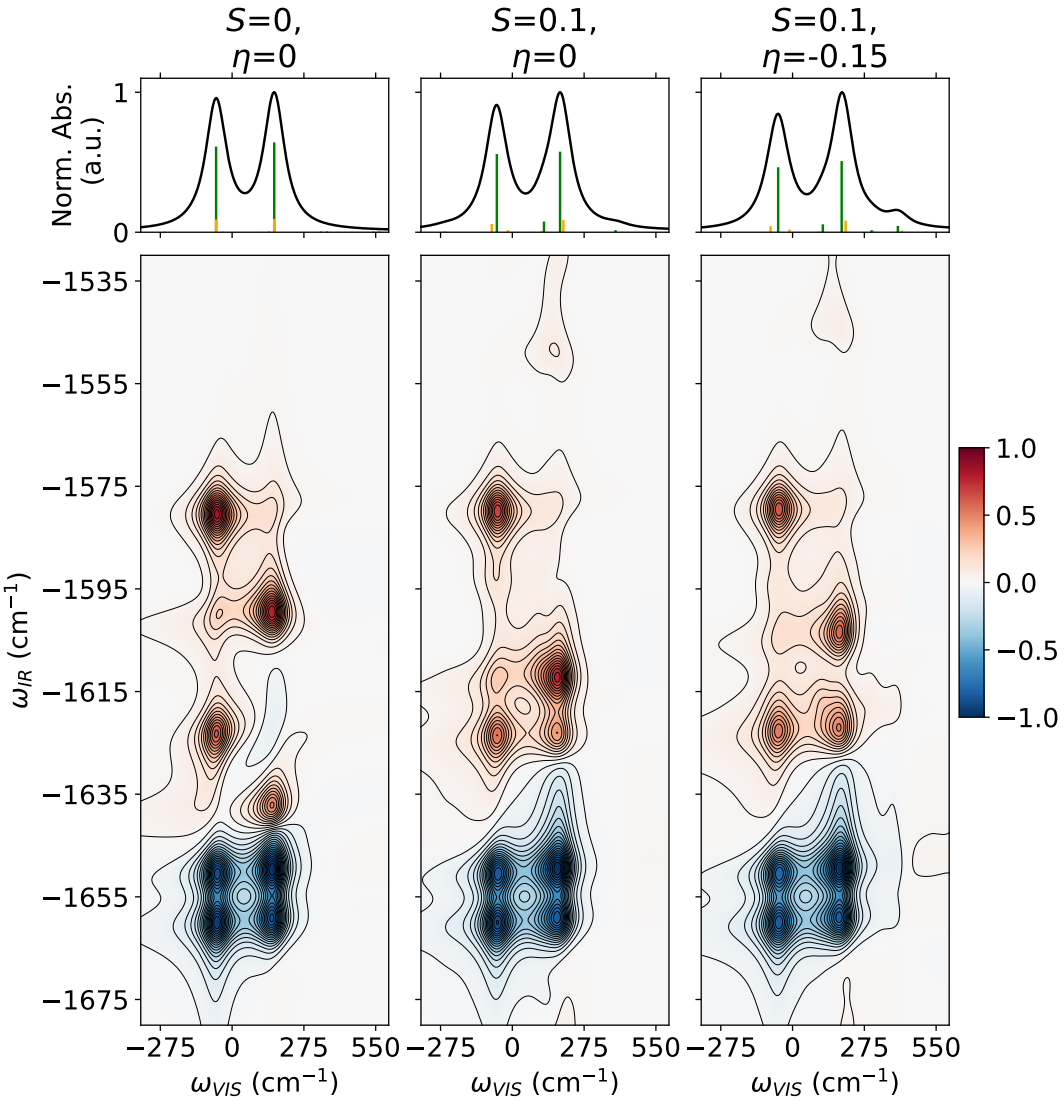

FIGURE 4.6: The ESE and GSE diagrams for identical parameters used in Fig. 4.5.

4.1.2 Dimer angle variation

As explained in section 2.2.7, different pulse polarisations can be used to investigate the (dimer) systems. The dimer system defined in Ref. [6] does not have an explicitly defined an angle between the chromophores: it is somehow absorbed in the ratio of the dipole moments. Hence the calculation so far (after the definition of the coupling and TDM ratio) is a one dimensional one in geometrical space. However, the angle can be varied explicitly, which is done in this section. An angle is introduced between the TDMs of the chromophores, keeping the excitonic coupling constant at 100 cm^{-1}, which could also have been varied, as the coupling and TDMs have the same physical dipoles at their origin, but that was not done here.

Two angles are investigated: 10° and 20°. 2DEV spectra are calculated for parallel and perpendicular setups and are subtracted. In line with the previous section, the same three vibronic cases are considered. The result for 10° is shown in Fig 4.7 and for 20° in 4.8. It is seen that specific peaks show a difference between the two polarisation setups, while others do not. Several observations can be made

- The 2DEV difference is larger for 10° than for 20°, as expected 'intuitively'.
- For both angles, in the GSB peaks only a prominent difference is seen in the peaks at $\omega_{IR} \approx 1660$ cm^{-1}, which correspond to the vibrational mode in the electric ground state on site A. The other two GSB peaks (corresponding to the vibrational mode in the ground state of site B) do not show a difference for either angle: the non-zero difference at those peak locations is thought to be the tail of the difference at $\omega_{IR} \approx 1660$ cm^{-1}.
- The most prominent difference is seen for two peaks in the left column: one is a GSB peak mentioned above: it shows the largest difference. The other is an ESA peak at $\omega_{IR} \approx 1620$ cm^{-1}.
- There is a clear distinction between peaks in this 2DEV subtraction within the individual vibronic cases. However, the difference between the vibronic cases is much less prominent in these subtractions.

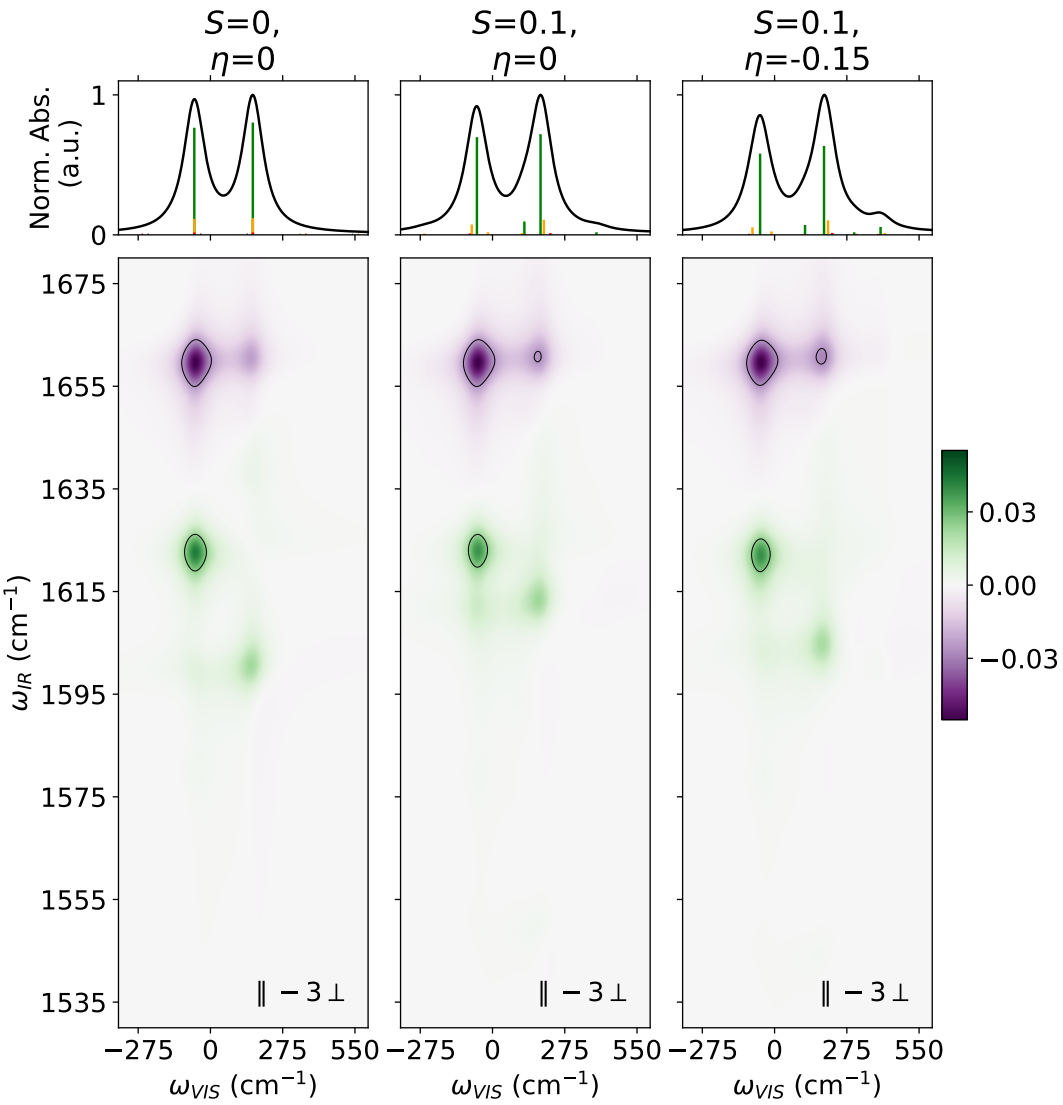

FIGURE 4.7: Shown is the difference between the 2DEV spectra calculated for two different pulse polarisations: "parallel" minus "three times perpendicular". An angle of 10° between the chromophore TDMs is introduced. These spectra are calculated using the same parameters as in Appendix A except for the new TDM angle. The vibrational and electronic transition dipoles are again assumed parallel per chromophore. A different colour scheme from previous figures is chosen to illustrate that these figures show a difference between 2DEV spectra. The contours are drawn at the same intervals, illustrating the relative magnitudes of the peak differences: largest difference is approximately 5%, relative to the highest peak in the 2DEV's in Fig. 4.4.

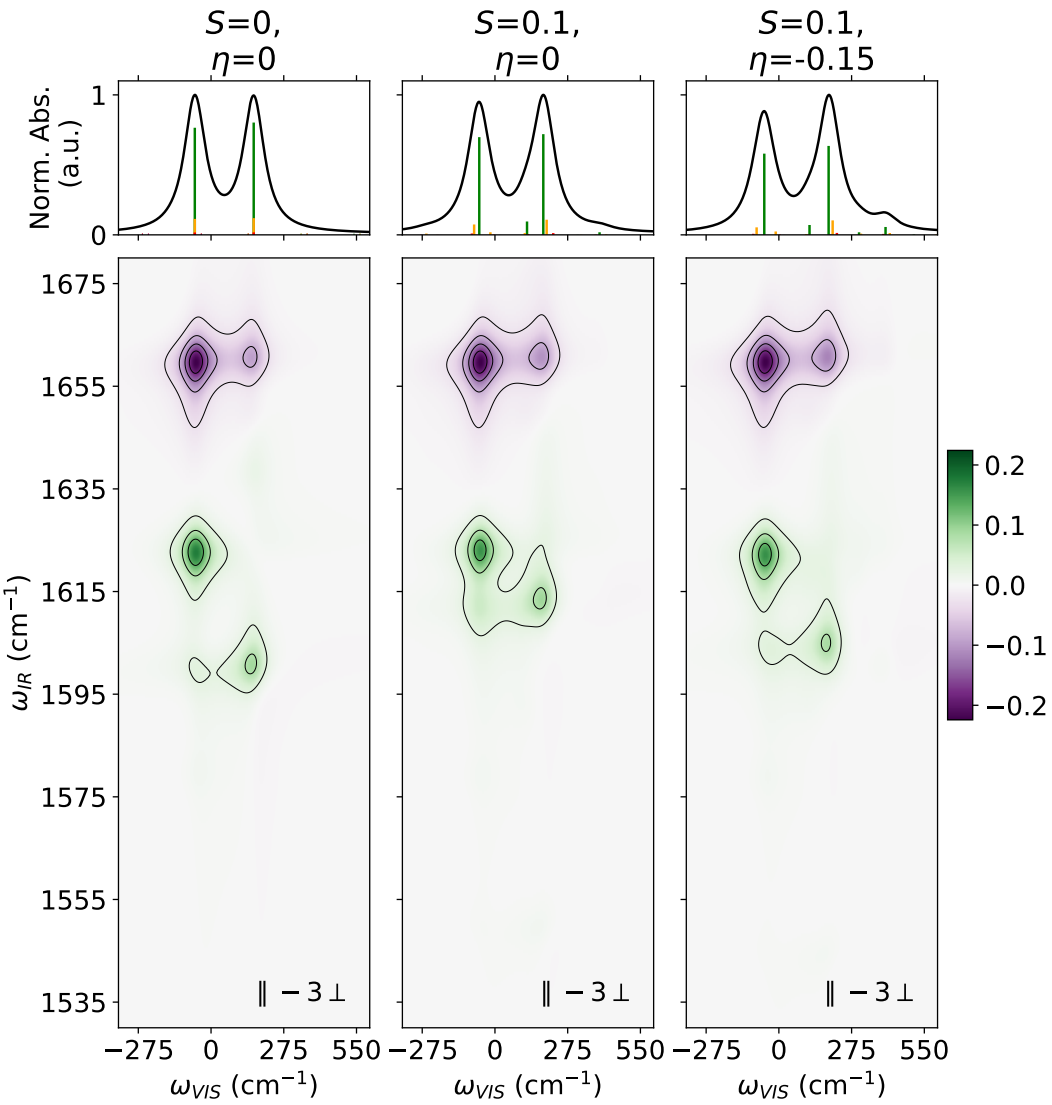

FIGURE 4.8: The same calculation as in Fig. 4.7 but with a larger angle between the transition dipole moments: 20°. The largest difference between the parallel and perpendicular signals is now approximately 20% compared to the highest peak in Fig. 4.4.

4.2 Homodimer

The previous section concerns a dimer that features only slight vibronic mixing (weak coupling): J was on the order of the excitonic gap, while the Huang Rhys factors and the parameter specifying the HT activity were small. In this section, a dimer with strong vibronic mixing character is discussed: the homodimer defined in Ref. [22, 23]. It has a larger Huang-Rhys factor ($S = 0.58$) and excitonic coupling ($J = 800$ cm^{-1}), see Appendix B.

Since for the heterodimer the vibronic mixing is quite weak, there is a strong correspondence between the eigenstates and site-states, meaning that the peaks in the 2DEV spectrum can be 'labelled' by describing the phenomena as if they involve transitions between site-states rather than eigenstates. This procedure is not valid for the homodimer's 2DEV spectrum, where the character of the individual sites is lost. As such, a less detailed description of the individual peaks in the 2DEV spectra will be given for the homodimer.

The energy fluctuations due to the dimer-bath coupling are shown in Fig. 4.9 for three difference trajectories (three different dimers in the ensemble) in order to get an impression of the bath implementation.

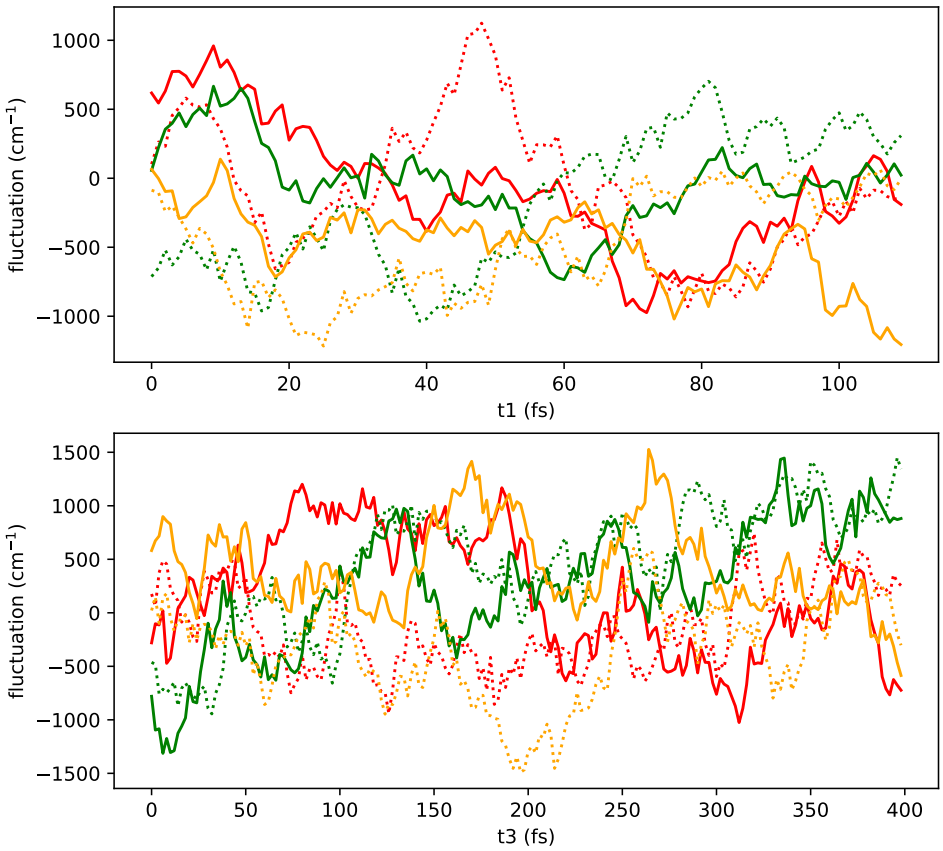

FIGURE 4.9: Shown are three noise trajectories for the exciton energies on the two dimer sites. Each color represents a different bath trajectory, while each linestyle represents a different exciton site: the continuous line site A and the dotted line site B. The waiting time t_2 is set to 100 fs in this case. During this waiting time the bath variations (δE_A and δE_B) are updated with a time resolution equal to that chosen for the t_3 interval. As the t_3 interval is longer than the t_1 interval, the energy fluctuations have a larger overall spread on t_3.

4.2.1 Basic 2DEV spectra

The first calculation discussed in this section is the homodimer's linear response, which is shown in Fig. 4.10. This is calculated to get an impression of the system's energy structure and to have a basic test of this work. There are no two distinct 'exciton' peaks seen in Fig. 4.10, which is due to the strong inter-site coupling. Instead, the system is vibronically mixed to the point that the individual sites are not recognisable. The response in Fig. 4.10 corresponds well to Figure 1b in Ref. [22], giving at least some assurance in the validity of this work's calculation. Additionally, the 'monomer spectrum' was verified, as seen in Appendix F, which is calculated for the same system by changing $J = 100$ cm^{-1} to zero.

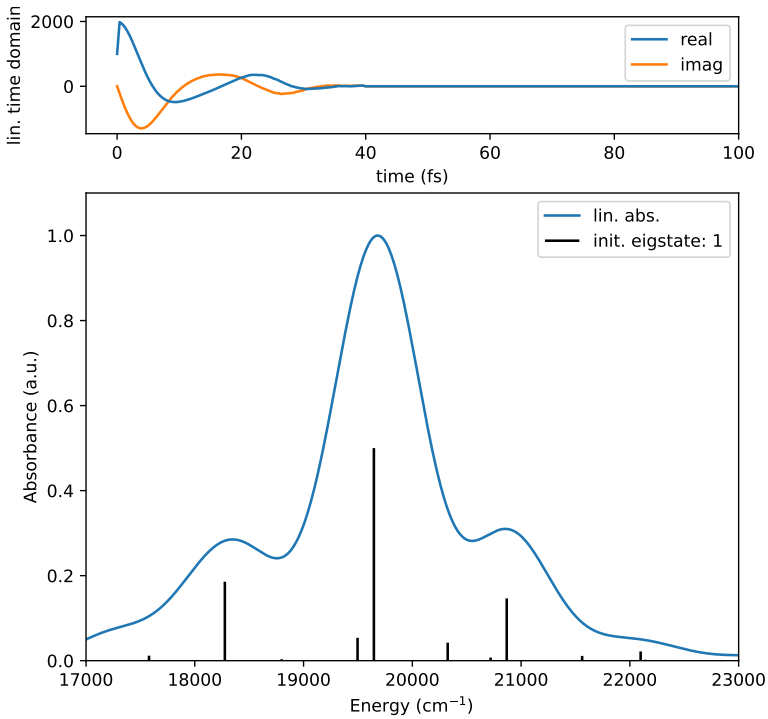

FIGURE 4.10: Shown is the linear absorption spectrum for the investigated homodimer. The top figure shows the linear response in time domain, which 'decays to zero' after approximately 50 fs. The bottom figure shows the linear response in frequency domain. The black vertical lines depict the stick spectrum, calculated without noise. Zero padding was applied to the time domain response signal for increased resolution, but only the initial 100 fs is shown where the signal is non-zero. (The "init. eigstate: 1" is administrative, denoting that the spectrum is calculated for the system in ground state; state index 1 and not 0 because of the exciton downshifting described in section 3.)

Having demonstrated the linear absorption spectrum, the 2DEV spectrum is calculated next, shown in Fig. 4.11. The left and middle columns of the figure show that the 2DEV response for all diagrams feature a line at a single value on the IR axis. That value is $\omega_{IR} = 1220$ cm^{-1}, the frequency of the vibrational mode in this homodimer. When starting this calculation, the possibility was anticipated that the strong vibrational coupling (Franck-Condon Factor $S = 0.58$) would cause more elaborate structure along the IR axis, but a more simple 2DEV spectrum is found instead. *This is a result in itself.*

To elaborate on this finding: contrary to the heterodimer investigated above, the homodimer has all vibrational modes with identical frequency in the electronic ground and excited manifolds. As noted before for the heterodimer, the splitting of the ESA and GSB 'peak groups' on the IR axis is attributed to the fact that the system features different vibrational mode frequencies in

the ground and excited manifolds. Further separation along the IR axis of the peaks within either GSB or ESA diagram type was attributed to the vibrational modes being slightly different for the two sites.

The vibrational modes in the homodimer are not different between ground and excited manifolds, nor are they different between either site A or B. Hence, no splitting occurs along the IR-axis and the different diagrams add up to zero, seen in the bottom row of Fig. 4.11: there are no peaks. In short, the finding that the signal adds up to zero is linked to the assumption that the vibrational modes are identical.

It is evident that the 2DEV 'spectral shape' is quite different for the different Feynman diagrams. Especially GSE stands out from the others.

Additionally, as can be seen in the right column of Fig. 4.11, barely a difference is found between the parallel and perpendicular 2DEV spectra (other than the overall factor 3).

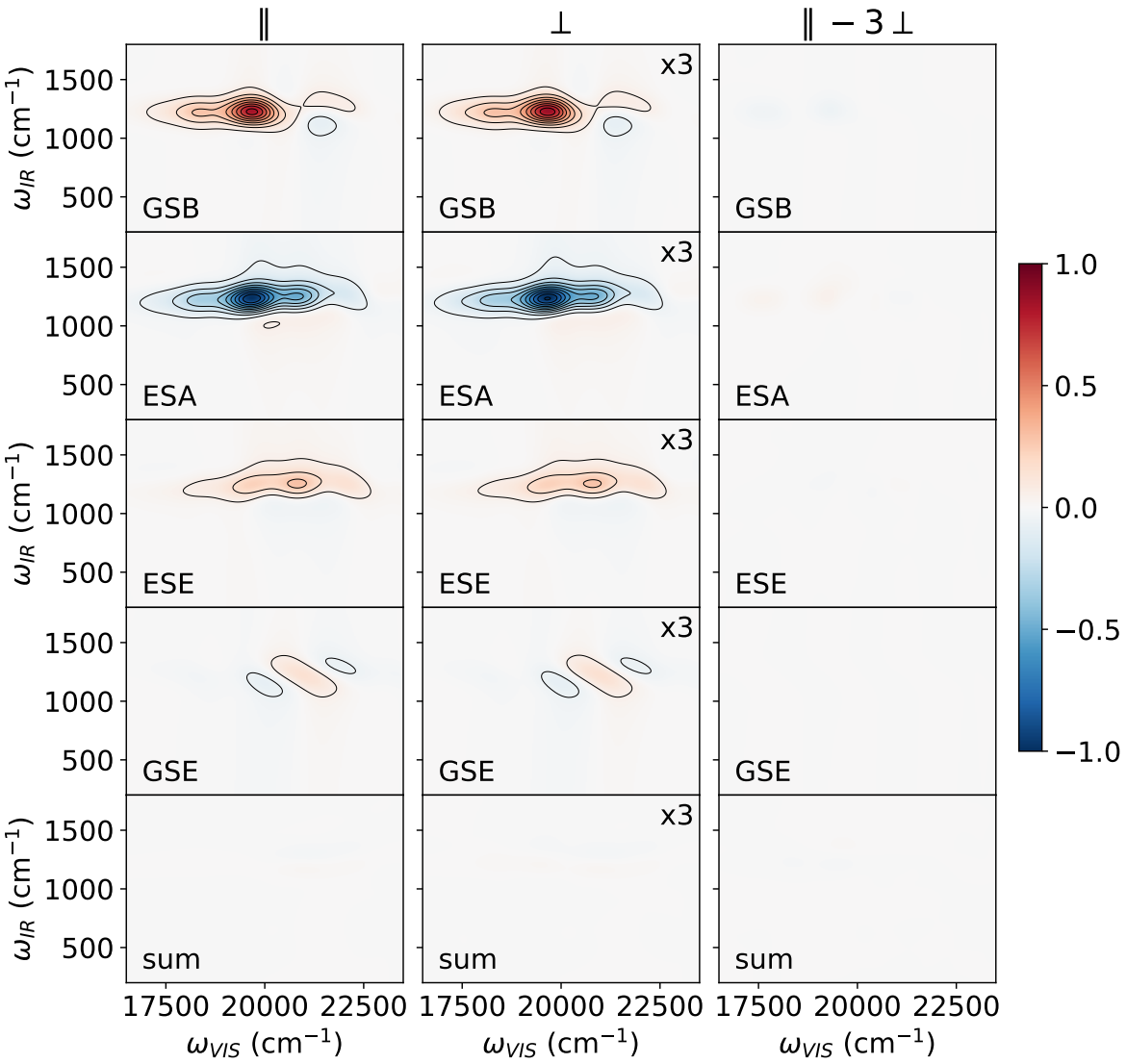

FIGURE 4.11: 2DEV spectra for the homodimer. Each row represents the labelled Feynman Diagram type, see. Fig. 2.2 for elaboration. The bottom row is the sum of all diagrams. The left column shows the 2DEV spectra for the configuration where all external magnetic fields are polarised in the same direction; the middle column shows the spectra for the configuration where the first two fields are polarised perpendicularly to the second two, multiplied by a factor 3; the right column shows the difference between the preceding columns, which is found to be approximately zero.

The colours represent the intensity (in arbitrary units) of the 2DEV spectra at the indicated combination of 'electronic' and infrared frequencies on the respective axes. The diagrams in each column get the same scaling factor: the left column is scaled to maximum absolute value one, which means the highest (negative) peak of the ESA diagram has an intensity of minus one; the middle column gets that same factor times an extra factor 3 for easy comparison, as elaborated in section 2.2.7.

The contours are plotted at intervals of 0.1. The rest of the specifics of the 2DEV spectra are summed up in Appendix B. The waiting time t_2 is zero.

Slices of the 2DEV spectra shown in Fig. 4.11 at $\omega_{\mathrm{IR}} = 1220$ cm^{-1} are shown in Fig. 4.12. Here it can more clearly be seen that there is hardly a difference between the parallel and perpendicular polarisation setups.

Of the different diagram types, the ESA shows a peak structure that has most overlap with the linear absorption, especially at frequencies below ~ 20500 cm^{-2}. Both GSB and ESA start deviating significantly from the linear absorption shape at that frequency. In line with the observation that the diagrams add up to zero, the GSB and ESA spectra 'lose' intensity to the GSE and ESE diagrams at higher frequencies.

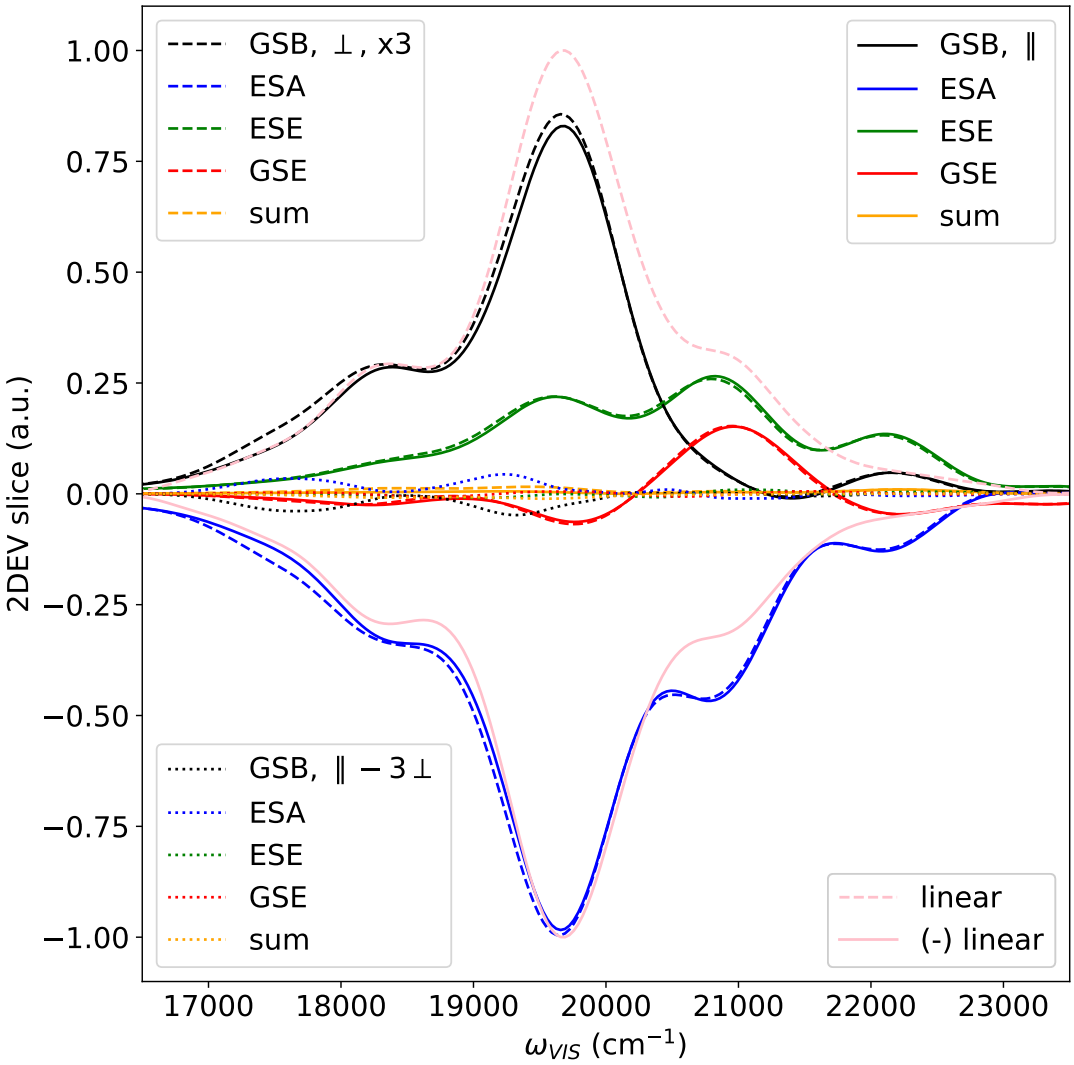

FIGURE 4.12: Shown is a slice at $\omega_{IR} = 1220\text{cm}^{-1}$ of all the 2DEV spectra and differences shown in Fig. 4.11. The scaling is kept the same. Each color represents a different Feynman diagram type. The solid lines depict the parallel setup, the dashed lines the perpendicular setup and the dotted lines depict the difference between those. In addition, the linear absorption spectrum is shown (both 'standard' and multiplied by a factor -1), for comparison with the 2DEV spectra shapes.

4.2.2 Three waiting times

The last computation to be discussed is the comparison of the homodimer's 2DEV spectra for several waiting times: three t_2 times. In Fig. 4.13, these times are varied in order to get an impression of the time evolution of the dimer. Following the order of magnitude in Figure 4 in Ref. [22], a waiting time up to 100 fs is chosen. The main conclusion here is that most of the spectral beats seem to happen at ω_{VIS} frequencies above ~ 20000 cm^{-1}, where the strongest GSE and ESE

signals are. The sum of the Feynman diagrams remains zero for the different waiting times.

Though it is not done in this work, the intensity at a single point in the 2DEV spectra could be traced as function of t_2. Additionally, the center line slopes could be investigated as function of the waiting time.

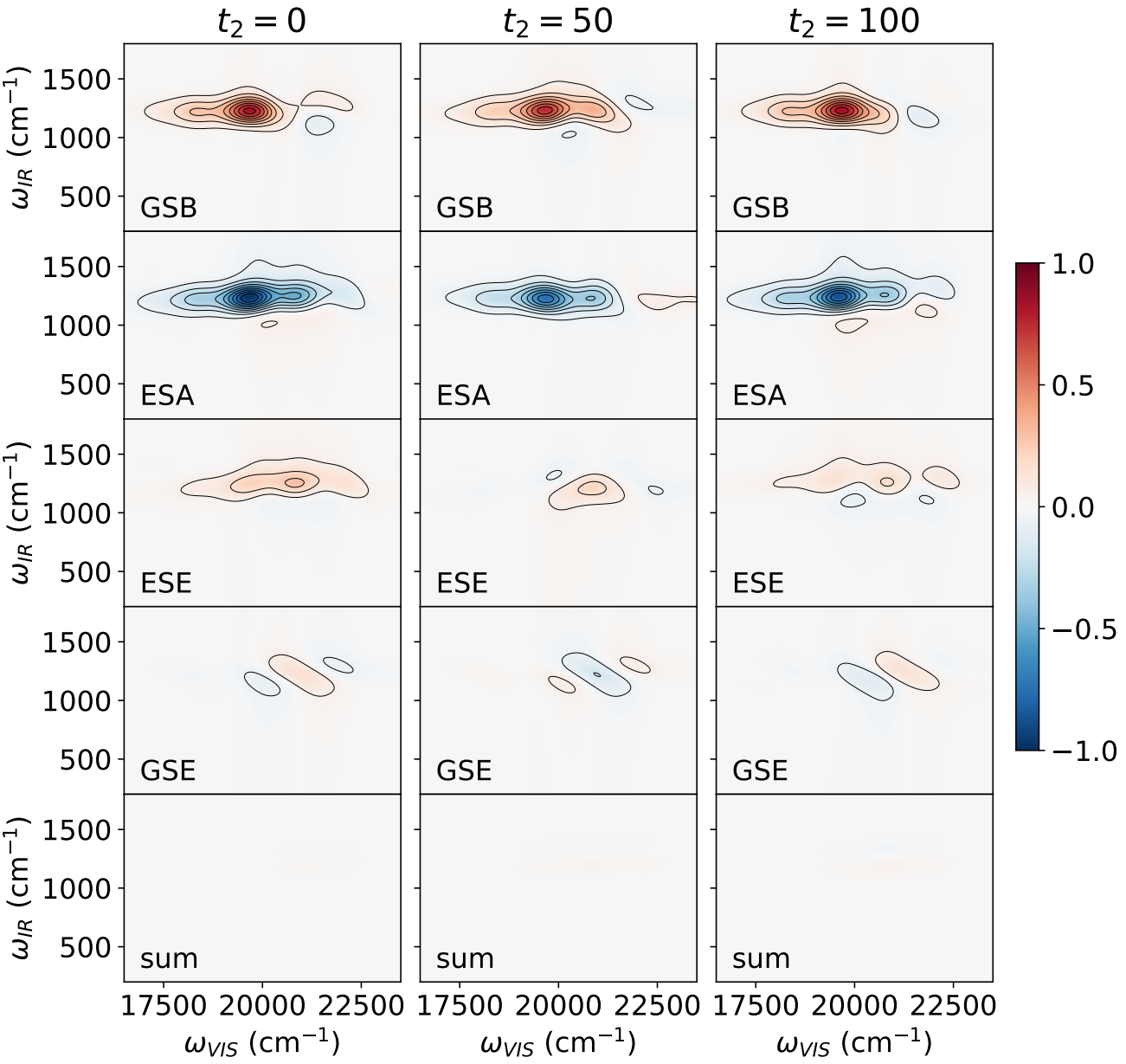

FIGURE 4.13: Shown are the 2DEV spectra for three different t_2 waiting times, the 'middle time interval', as defined in Fig. 2.2. The waiting times are 0, 50 and 100 fs respectively. The colourbar is identical to that in Fig. 4.11.

Chapter 5

Discussion

In this Chapter, several aspects to the validity and reliability of this work's results are discussed qualitatively. More specifically, several sources of uncertainty are explained. As is the case for many computational investigations, there is a trade-off in the implemented model's complexity/elaborateness and the sub-sequential computational cost. Uncertainty arises both from the chosen theoretical framework and from approximations within that framework.

5.1 Uncertainty inherent to the applied theory

In this work, dimers with various basic properties are investigated. The relevance of the chosen systems is as follows: the heterodimer features a basis set that covers the most simple case of a dimer that includes both Franck-Condon and Herzberg-Teller activity, particularly in the fact that only one chromophore accommodates these activities in its low frequency mode. While real life systems are not expected to be limited to this simple configuration, this is the simplest case to investigate these two activities. For instance, real life systems could feature both these vibronic activities over a chain of chromophores. Hence this limitation immediately suggests future interesting investigations.

Additionally, in the homodimer it is assumed that all vibrational modes are identical. As seen, this assumption leads to the total 2DEV spectrum being a zero signal. Moreover, basic assumptions such as the dipole-dipole approximation, delta-pulse envelope, zero temperature in the homodimer, accommodation of a single electronic excitation are made in the 2DEV calculation, all of which assume some 'ideal' scenario in their respective aspects.

It is worth noting that in the calculations of this work, no bath coupling is added in the main investigation of the heterodimer and that for the homodimer investigations only the two exciton energies are fluctuated. Of course in real systems, the vibrational modes and couplings between energy levels also fluctuate.

5.2 Errors due to finite computation time

Aside from theoretical approximations as above, an explicit error analysis on the uncertainty in the 2DEV spectra in this work would involve calculating many 2DEV spectra to investigate how sensitive they are to specific parameter changes. Such analysis is not done in this work, yet some description of reasons for uncertainty can be given.

Errors/uncertainties in the calculation are introduced by truncations that are necessary in order to limit computation time. Things that directly relate to computational cost and precision are:

1. 2D time grid size, refining this is a bit of an art. Additionally, the zero padding on the time domain 2DEV response introduces slight artefacts in the form of 'ripples' on the peaks, as the peaks are convoluted with sinc functions. These are eliminated as far as possible, but should be mentioned.

2. Number of Feynman diagrams included in the calculation. All possibilities were included, but for the heterodimer, the GSE and ESE diagrams did not yield extra information compared to GSB and ESA.

3. Choosing the Hamiltonian size necessarily introduces basis truncation artefacts, specifically because of the number of vibrational quanta allowed in the total system. In case of large Huang-Rhys factors, as in the homodimer, 2DEV peaks are shifted for 'small' basis sets, as seen in Appendix G. Initially there was confusion in the 2DEV findings, because the basis set chosen for the analysis of the homodimer was a bit too small. It could accommodate 7 vibrational excitations in the entire system, which lead to additional peaks that were not quite understood. Moreover, all Feynman diagrams did not quite add up to zero. As such, it is tricky to guess which artefacts remain as the result of the chosen final basis set.

4. While the implementation of non-zero temperature effects introduces uncertainty in the 2DEV spectra, as not all states are chosen to be occupied initially,

5. The number of realisations added to arrive at a 2DEV response of a realistic ensemble is chosen as a compromise between computational tractability and accuracy. Inherently, less noise is present for a higher number of trajectories.

5.3 Specific 2DEV findings

A few remaining comments of the differences between this work's 2DEV heterodimer spectra and those in Ref. [6] are the following.

- The fact that the different vibronic cases show a less prominent difference around the 400-500 cm^{-1} region in Fig. 4.4 than in 4.1 is not fully understood. The linear absorption in Fig.

4.4 shows the 'bulge' in that regime for the FC and HT cases, but the 2DEV does not seem to do so 'sufficiently'. It was considered that the temperature was not implemented properly in the sense that higher energy initial system states were not contributing. However, that does not seem to be the explanation, as the corresponding 'bulge' in the linear absorption for the HT case in Fig. 4.4 is due to the lowest initial energy state.

- The system-bath implementation in Ref. [6] leads to a shift on the IR axis of the 2DEV spectra that is not found in this work. It was investigated whether this work's bath implementation, based on fluctuating system energy levels, could also account for such a shift. That was done by trying several noise variations on the vibrational energy levels that would approximately recover the peak widths in the original work. Yet, these fluctuations did not yield a shift on the IR axis of the peaks, as expected.

- Slightly different definitions of the vibrational TDM, the one in this work taking the displacement in excited state into account, could explain some of the slight remaining differences between the heterodimer 2DEV spectra in this work and those in Ref. [6], but this is not investigated specifically.

Chapter 6

Conclusion

In this work, a 2DEV calculation method was implemented and applied to two types of dimer systems in order to contribute to the theoretical background of 2DEV spectroscopy, a relatively new technique. Three goals were set in this work 1) to verify the basic results of 2DEV work on a heterodimer [6], 2) to expand on those results by including laser polarisation in the calculation and 3) to use calculate 2DEV spectra for a homodimer with strong vibronic coupling that had not been investigated with 2DEV previously.

The first goal was achieved in the sense that basic features of GSB and ESA peaks were reproduced: two columns of peaks were found, which verified the previous work in Ref. [6] qualitatively. Moreover, the four GSB peaks were found to match, except for a shift of approximately 5 cm^{-1} on the IR-axis. This same shift was also found for the ESA peaks. This shift is attributed to the difference in the specific system-bath implementation between this work and the original. The original work shows features in the region from $\omega_{\mathrm{VIS}} = 400\text{-}500\ \mathrm{cm}^{-1}$ of the 2DEV spectra for the vibronic cases when Franck-Condon and Herzberg-Teller activity are present. This is reproduced to some degree, but the found 2DEV features in that region are much less prominent than in the original work.

The second goal of this work was achieved by introducing an angle between the heterodimer's two different chromophore transition dipole moments. Two of these 'dimer angles' were investigated (10° and 20°) by computing 2DEV spectra, assuming two different polarisation setups of the external electromagnetic fields: perpendicular and parallel. The difference between these spectra yielded a '2DEV subtraction' that manifests itself clearly for certain peaks, but not for others. Most notably, the 2DEV difference is larger for the larger angle, as expected. Additionally, the 2DEV peaks belonging to the lower energy 'exciton' excitation shows a larger dependence than the higher energy 'exciton'.

The third goal was achieved already by calculating the 2DEV spectra for the dimer defined in Ref. [22]. While in the heterodimer the peaks of the different Feynman diagrams did not overlap due to the dimer's specifics, this was not the case for the homodimer. As such, the 2DEV peaks

were found on a single value of the IR-axis: at the vibrational quantum of the harmonic oscillator in the homodimer. The non-zero Franck-Condon activity does not cause a splitting of 2DEV peaks along the IR-axis. As a result, the total sum of all the Feynman diagrams is zero: the 2DEV signal that would be measured for the homodimer is zero under the made assumptions. In other words, a difference in vibrational frequency between the ground state and excited state is crucial for generating a 2DEV signal and strong vibronic coupling alone (of Franck Condon type) does not induce a 2DEV signal.

The findings of this thesis outlined above lead to new interesting research questions. This work can be expanded upon in various ways. The investigated dimer had the 'strong' vibronic activity in a mode that was off-resonance with the 2DEV probe, while the homodimer had the 'strong' vibronic activity in a mode that was on-resonance with the 2DEV probe. It would be interesting to investigate the direct influence of having the 2DEV on- or off-resonance with the strongly coupled vibrational mode. This might be done by defining a single dimer system with two vibrational modes, one of which has strong vibrational coupling, and calculating 2DEV spectra for two different regions on the IR axis, which is achieved by using the distinct modes' TDM operators.

One reason for the relevance of this work is the role of vibrational coupling in exciton/energy transport in natural light harvesting systems, organic photovoltaics etcetera. Such energy transport happens in molecular aggregates and systems larger than a dimer. Hence it is interesting to extend the calculations in this work to a trimer or larger, rather than dimer only: the mathematics and computer code are readily extendable. It is interesting to check how the difference between vibronic cases changes when extending the molecular chain. This is more expensive than the dimer calculation, but in case of relatively weak coupling, the number of vibrational states need not be large. As such the Hilbert space dimension can remain relatively low and so these computations are expected to be tractable.

Chapter 7

Acknowledgement

I should be grateful to more people than I can probably fit on this page, but I will make an attempt. First and foremost, I am grateful to my supervisor who helped me set up the calculations, interpret my findings and understand concepts that were new to me. Additionally, I thank him for being patient with me. At times, my research felt like a struggle and Thomas encouraged me in a few crucial moments. Many thanks to professor Pchenitchnikov for taking the time to examine my work. I thank Eric Arsenault for confirming our suspicion about the calculation discrepancy and for elaborating on the remaining IR-axis difference.

Marick Manrho deserves a special thanks for providing a tutorial during our 'Coffee Code Club' on programming Holstein Hamiltonians, which helped me understand how these systems are implemented in computer code. I am grateful to my friend Hans, for helping me prepare my final presentation by attending my less than 'dress rehearsal' and by providing useful feedback for my talk.

I thank my friend Lisa for keeping me company during training sessions over the past year, which proved a nice break from studying. Of course I thank my office mate Ivo for excellent conversation, a good dose of humour, sharing of musical interest, friendship and a quality blackboard drawing of me in my natural state. Cheers man, all the best! Thank you Vesna, for our great conversations, for letting people feel welcome in the office and for creating a sense of community there. I am sure you will keep doing that wherever you end up working.

I thank my family for all their support throughout my studies. For that I also thank my friends Reinier and Marcel.

Doing theoretical work without too many co-workers can be a solitary occupation and at times I found that a bit lonely. Therefore, I very much liked the group's tradition of bringing cake to the group meetings and of having lunch together as often as possible.

How can I end this thesis without thanking the other lovely people with whom I spent the past year in the office: Evgenii, Alba, Thomas, Ceyda, Johannes, Tenzin, Kai, Elisa, Arunesh and others. I felt welcome on the theory hallway and I wish you all the best further in life.

Bibliography

[1] Qingzhen Bian et al. "Vibronic coherence contributes to photocurrent generation in organic semiconductor heterojunction diodes". In: *Nature Communications* 11.1 (2020), p. 617.

[2] Hou-Dao Zhang, Qin Qiao, R. Xu, and Yijing Yan. "Effects of Herzberg-Teller vibronic coupling on coherent excitation energy transfer." In: *The Journal of Chemical Physics* 145 20 (2016), p. 204109.

[3] Hong-Guan Duan, Peter Nalbach, Robert J. Dwayne Miller, and Michael Thorwart. "Intramolecular vibrations enhance the quantum efficiency of excitonic energy transfer." In: *Photosynthetic Research* 144 (2020), pp. 137–145.

[4] Justin R. Caram, Andrew F. Fidler, and Gregory S. Engel. "Excited and ground state vibrational dynamics revealed by two-dimensional electronic spectroscopy". In: *The Journal of Chemical Physics* 137.2 (2012), p. 024507.

[5] Eric A. Arsenault, Pallavi Bhattacharyya, Yusuke Yoneda, and Graham R. Fleming. "Two-dimensional electronic–vibrational spectroscopy: Exploring the interplay of electrons and nuclei in excited state molecular dynamics". In: *The Journal of Chemical Physics* 155.2 (2021), p. 020901.

[6] Eric A. Arsenault, Addison J. Schile, David T. Limmer, and Graham R. Fleming. "Vibronic coupling in energy transfer dynamics and two-dimensional electronic–vibrational spectra". In: *The Journal of Chemical Physics* 155.5 (2021), p. 054201.

[7] Thomas A. A. Oliver, Nicholas H. C. Lewis, and Graham R. Fleming. "Correlating the motion of electrons and nuclei with two-dimensional electronic-vibrational spectroscopy". In: *Proceedings of the National Academy of Sciences* 111.28 (2014), pp. 10061–10066.

[8] Eric C. Wu, Eric A. Arsenault, Pallavi Bhattacharyya, Nicholas H. C. Lewis, and Graham R. Fleming. "Two-dimensional electronic vibrational spectroscopy and ultrafast excitonic and vibronic photosynthetic energy transfer". In: *Faraday Discussions* 216 (0 2019), pp. 116–132.

[9] Trevor L. Courtney, Zachary W. Fox, Karla M. Slenkamp, and Munira Khalil. "Two-dimensional vibrational-electronic spectroscopy". In: *The Journal of Chemical Physics* 143.15 (2015), p. 154201.

[10] Trevor L. Courtney, Zachary W. Fox, Laura Estergreen, and Munira Khalil. "Measuring Coherently Coupled Intramolecular Vibrational and Charge-Transfer Dynamics with Two-Dimensional Vibrational–Electronic Spectroscopy". In: *The Journal of Physical Chemistry Letters* 6.7 (2015), pp. 1286–1292.

[11] Kritanjan Polley and Roger F. Loring. "2D electronic-vibrational spectroscopy with classical trajectories". In: *The Journal of Chemical Physics* 156.20 (2022), p. 204110.

[12] Pallavi Bhattacharyya and Graham R. Fleming. "Two-Dimensional Electronic–Vibrational Spectroscopy of Coupled Molecular Complexes: A Near-Analytical Approach". In: *The Journal of Physical Chemistry Letters* 10.9 (2019), pp. 2081–2089.

[13] Nicholas H. C. Lewis and Graham R. Fleming. "Two-Dimensional Electronic-Vibrational Spectroscopy of Chlorophyll a and b". In: *The Journal of Physical Chemistry Letters* 7.5 (2016), pp. 831–837.

[14] Thomas A. A. Oliver and Graham R. Fleming. "Following Coupled Electronic-Nuclear Motion through Conical Intersections in the Ultrafast Relaxation of β-Apo-8'-carotenal". In: *The Journal of Physical Chemistry B* 119.34 (2015), pp. 11428–11441.

[15] Eric C. Wu, Qinghui Ge, Eric A. Arsenault, Nicholas H. C. Lewis, Natalie L. Gruenke, Martin J. Head-Gordon, and Graham R. Fleming. "Two-dimensional electronic-vibrational spectroscopic study of conical intersection dynamics: an experimental and electronic structure study". In: *Physical Chemistry Chemical Physics* 21 (26 2019), pp. 14153–14163.

[16] Nicholas H. C. Lewis, Hui Dong, Thomas A. A. Oliver, and Graham R. Fleming. "Measuring correlated electronic and vibrational spectral dynamics using line shapes in two-dimensional electronic-vibrational spectroscopy". In: *The Journal of Chemical Physics* 142.17 (2015), p. 174202.

[17] James D. Gaynor, Alessio Petrone, Xiaosong Li, and Munira Khalil. "Mapping Vibronic Couplings in a Solar Cell Dye with Polarization-Selective Two-Dimensional Electronic–Vibrational Spectroscopy". In: *The Journal of Physical Chemistry Letters* 9.21 (2018), pp. 6289–6295.

[18] James D. Gaynor, Robert B. Weakly, and Munira Khalil. "Multimode two-dimensional vibronic spectroscopy. I. Orientational response and polarization-selectivity". In: *The Journal of Chemical Physics* 154.18 (2021), p. 184201.

[19] Robert B. Weakly, James D. Gaynor, and Munira Khalil. "Multimode two-dimensional vibronic spectroscopy. II. Simulating and extracting vibronic coupling parameters from polarization-selective spectra". In: *The Journal of Chemical Physics* 154.18 (2021), p. 184202.

[20] Minhaeng Cho (editor). *Coherent Multidimensional Spectroscopy*. Springer Singapore, 2019.

[21] James D. Gaynor, Jason Sandwisch, and Munira Khalil. "Vibronic coherence evolution in multidimensional ultrafast photochemical processes". In: *Nature Communications* 10.1 (2019), p. 5621.

[22] Alexei Halpin, Philip J. M. Johnson, Roel Tempelaar, R. Scott Murphy, Jasper Knoester, Thomas L. C. Jansen, and Robert J. Dwayne Miller. "Two-dimensional spectroscopy of a molecular dimer unveils the effects of vibronic coupling on exciton coherences". In: *Nature Chemistry* 6.3 (2014), pp. 196–201.

[23] Alexei Halpin, Philip J. M. Johnson, Roel Tempelaar, R. Scott Murphy, Jasper Knoester, Thomas L. C. Jansen, and Robert J. Dwayne Miller. "Supplementary material to "Two-dimensional spectroscopy of a molecular dimer unveils the effects of vibronic coupling on exciton coherences"". In: *Nature Chemistry* 6.3 (2014), pp. 196–201.

[24] Peter Hamm and Martin Zanni. *Concepts and Methods of 2D Infrared Spectroscopy*. Cambridge University Press, 2011.

[25] Shaul Mukamel. *Principles of nonlinear optical spectroscopy*. Engels. Oxford series in optical and imaging sciences ; 6. New York: Oxford University Press, 1995.

[26] Thomas L. C. Jansen. *Lecture notes for "Ultrafast Time-Resolved Spectroscopy"*. University of Groningen. 2020.

[27] Anna S. Bondarenko, Jasper Knoester, and Thomas L.C. Jansen. "Comparison of methods to study excitation energy transfer in molecular multichromophoric systems". In: *Chemical Physics* 529 (2020), p. 110478.

[28] James D. Gaynor and Munira Khalil. "Signatures of vibronic coupling in two-dimensional electronic-vibrational and vibrational-electronic spectroscopies". In: *The Journal of Chemical Physics* 147.9 (2017), p. 094202.

[29] Jun J. Sakurai and Jim Napolitano. *Modern Quantum Mechanics*. 2nd ed. Cambridge University Press, 2017.

[30] Robin M. Hochstrasser. "Two-dimensional IR-spectroscopy: polarization anisotropy effects". In: *Chemical Physics* 266.2 (2001), pp. 273–284.

[31] Thomas L. C. Jansen and Jasper Knoester. "Waiting Time Dynamics in Two-Dimensional Infrared Spectroscopy". In: *Accounts of Chemical Research* 42.9 (2009), pp. 1405–1411.

Appendix

A Parameters used in the heterodimer calculation

Most of these dimer parameters/specifics are directly copied from Ref. [6] (if available). Some, such as the dimer angle are introduced here.

Dimer parameters		
Parameter	Symbol	Magnitude
Dimer angle	θ	$[0°, 10°, 20°]$
Average electronic transition energy	ϵ	Kept zero
Excitonic gap	ΔE	100 cm^{-1}
Excitonic coupling	J	$\pm$100 cm^{-1}
Electronic TDM ratio	μ_{Ae}/μ_{Be}	$-1/4$
Vibrational TDM ratio	μ_{Av}/μ_{Bv}	1
On-resonance vibrational quantum, ground manifold A	$\hbar\omega_{\mathrm{A,g,f}}$	1650 cm^{-1}
On-resonance vibrational quantum, ground manifold B	$\hbar\omega_{\mathrm{B,g,f}}$	1660 cm^{-1}
On-resonance vibrational quantum, excited manifold A	$\hbar\omega_{\mathrm{A,e,f}}$	1545 cm^{-1}
On-resonance vibrational quantum, excited manifold B	$\hbar\omega_{\mathrm{B,e,f}}$	1540 cm^{-1}
Off-resonance vibrational quantum, A	$\hbar\omega_{\mathrm{A,s}}$	200 cm^{-1}
Max nr. of off-resonance mode quanta	ν_{MAX}	3
Huang-Rhys factor, all on-resonance modes	S_f	0.005
Huang-Rhys factor, off-resonance mode	S_s	$[0, 0.1]$
HT activity strength	η	$[0, -0.15]$
Dimer temperature	kT	105 cm^{-1}
Hamiltonian size	N_H	36
Other 2DEV parameters		
Parameter	Symbol	Magnitude
t_1 time resolution	dt_1	20 fs
t_1 array length	Nt_1	130
t_3 time resolution	dt_3	7 fs
t_3 array length	Nt_3	1100
Waiting time	t_2	0 fs
Zero padded t_1 array size	Nt_1^*	1000
Zero padded t_3 array size	Nt_3^*	10000
Gaussian apodisation on t_1	σ_1	500 fs
Gaussian apodisation on t_3	σ_3	3000 fs
Exponential apodisation on t_1	Γ_1	120 fs
Exponential apodisation on t_3	Γ_3	1800 fs

B Parameters used in the homodimer calculation

Most of these dimer parameters are directly copied from Ref. [23] (if available).

Homodimer parameters		
Parameter	Symbol	Magnitude
Dimer angle	θ	15°
Average electronic transition energy	ϵ_0	18190 cm^{-1}
Excitonic coupling	J	800 cm^{-1}
Electronic TDM ratio	μ_{Ae}/μ_{Be}	1
Vibrational TDM ratio	μ_{Av}/μ_{Bv}	1
Vibrational quantum	ω_0	1220 cm^{-1}
Max nr. of vibrational quanta allowed in dimer	ν_{MAX}	8
Huang-Rhys factor	λ^2	0.58
Solvent standard deviation	σ	500 cm^{-1}
Solvent correlation time	t_c	40 fs
Dimer temperature	kT	0 cm^{-1}
Hamiltonian size	N_H	135
Other 2DEV parameters		
Parameter	Symbol	Magnitude
Number of averaged trajectories	N_{real}	1000
t_1 time resolution	dt_1	1 fs
t_1 array length	Nt_1	110
t_3 time resolution	dt_3	2 fs
t_3 array length	Nt_3	200
Waiting time	t_2	$[0, 50, 100]$ fs
Zero padded t_1 array size	Nt_1^*	1000
Zero padded t_3 array size	Nt_3^*	10000
Gaussian apodisation on t_1	σ_1	25 fs
Gaussian apodisation on t_3	σ_3	70 fs
Exponential apodisation on t_1	Γ_1	N/A
Exponential apodisation on t_3	Γ_3	N/A

C Initial attempt at heterodimer 2DEV reproduction

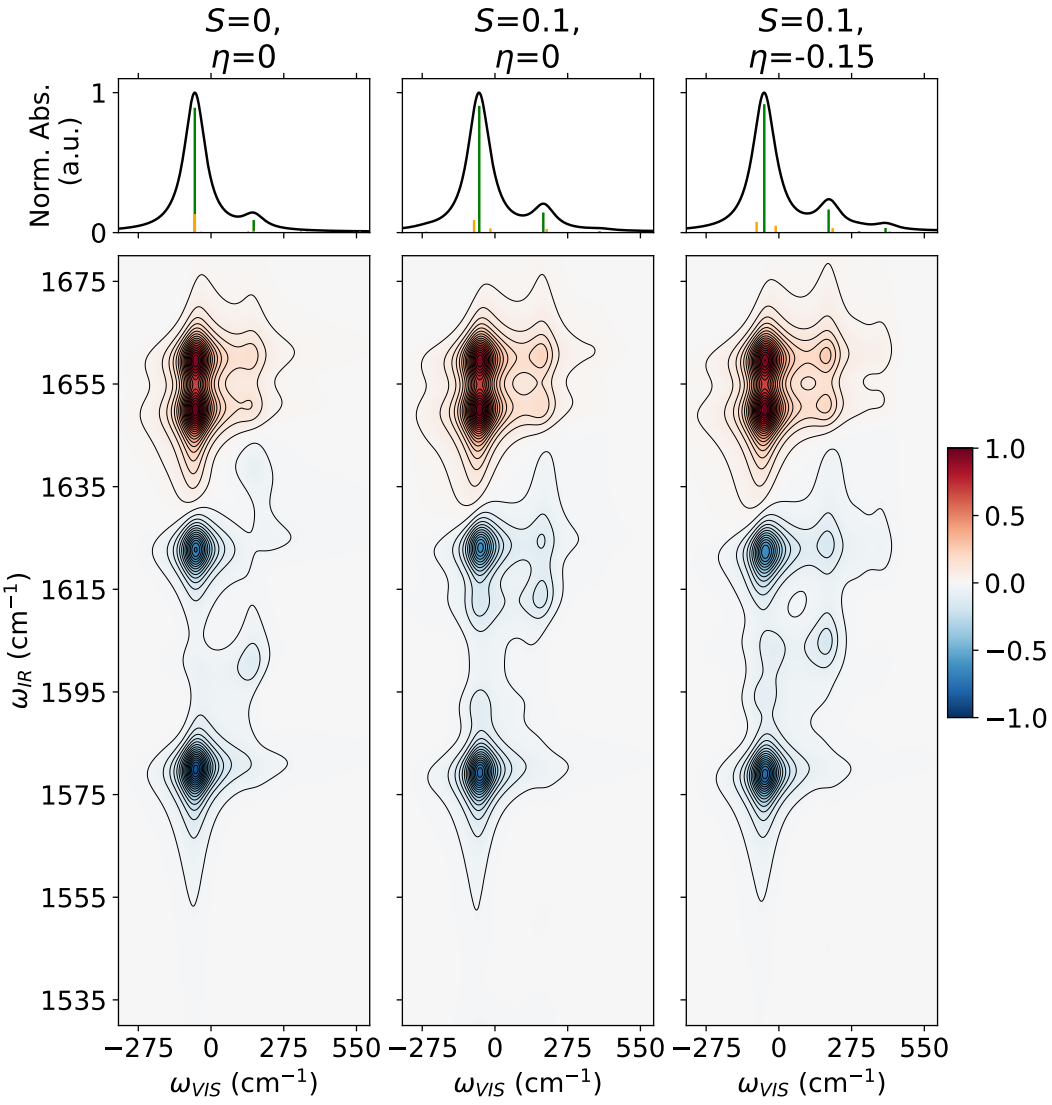

FIGURE *C1*: Initial attempt at reproducing the 2DEV spectra for the same three vibronic cases discussed in Ref. [6], seen in 4.1. As mentioned in the main text, the left/right peak ratio differs from that published in Ref. [6], is found for all three vibronic cases and is therefore most likely rooted in the 'electronic parameters' of the calculation.

D Slice of log peak ratio figure

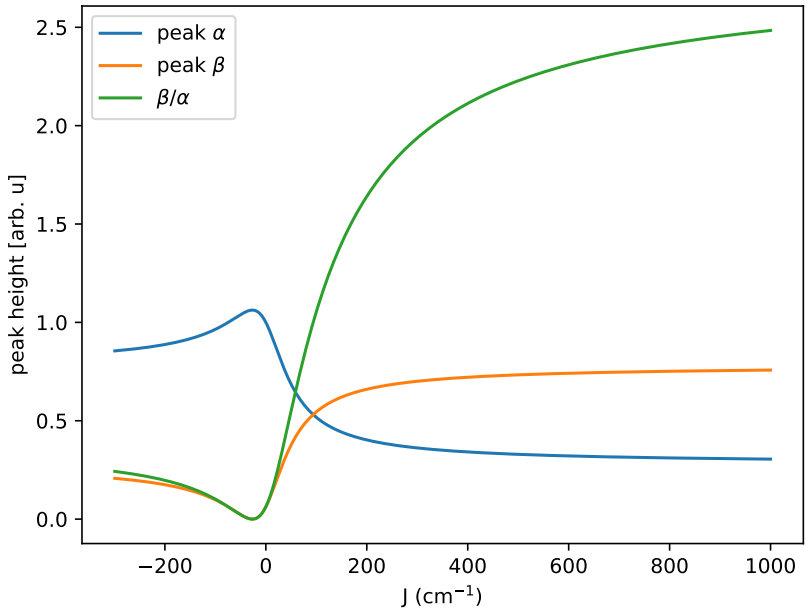

FIGURE *D1*: A slice at $\mu_B = 4\mu_A$ of the peak ratio as function of coupling and dipole ratio shown in Fig. 4.3. Here, the vertical axis represents both the individual peak intensities (a.u.) from 0 to 1; and the ratio between these, as indicated. As mentioned, the excitonic gap is 100 cm^{-1}. Note that at $\mu_B = 4\mu_A$ and $J = 100$, the peak ratio is approximately one.

E Noise on the heterodimer

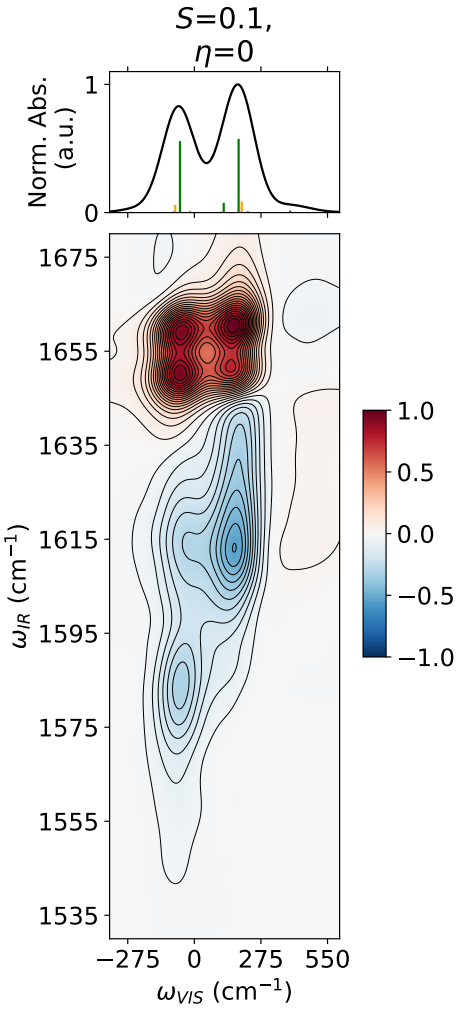

FIGURE *E1*: The 2DEV spectrum for the heterodimer FC case (middle vibronic case) with noise on the energy levels of the system. The timescale chosen for the bath fluctuation is $\Lambda = 50$ fs. The excitons have an independent fluctuation of $\sigma = 80$ cm^{-1}. The high frequency vibrational modes (on resonance with the 2DE**V** probe) are all given independent fluctuations of $\sigma_f = 10$ cm^{-1}, while the low frequency mode gets $\sigma_S = 2$ cm^{-1}. 200 trajectories are averaged in this spectrum. The exponential apodisations of $\Gamma_1 = 1/600$ fs^{-1} and $\Gamma_3 = 1/9000$ fs^{-1} and Gaussian apodisations of $\sigma_1 = 100$ fs and $\sigma_3 = 1600$ fs are put on the time domain response. This is *sufficient to demonstrate that the GSB peaks do not shift on the IR-axis in this bath implementation* for noise that cause peak widths of the same order as those in Fig. 4.1.

F Monomer spectrum (for homodimer model)

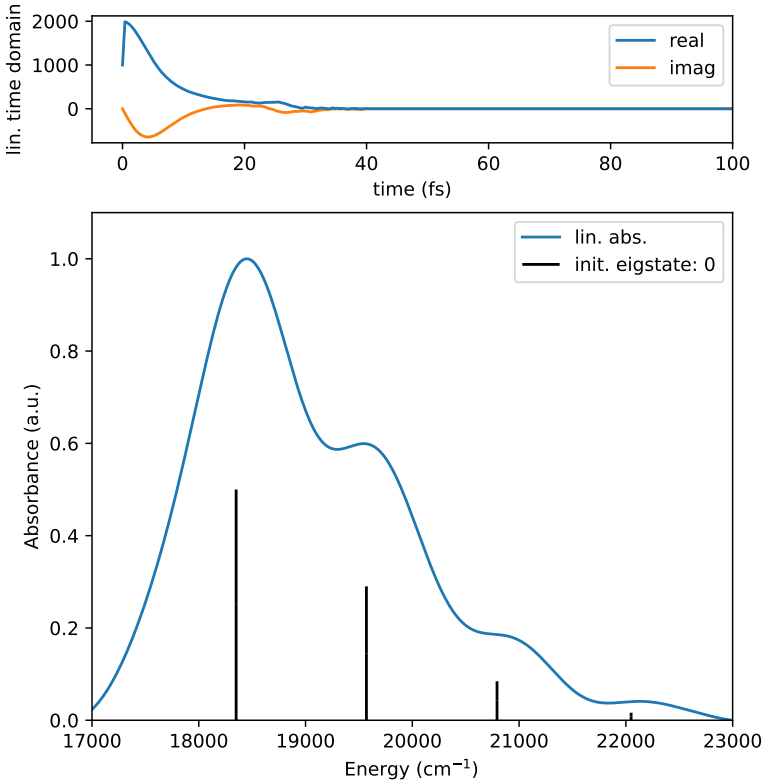

FIGURE *F1*: Shown is the linear response of the monomer, which is the homodimer system with the excitonic coupling J set to zero. The plot layout is the same as in Fig. 4.10: the top graph displays the response function in time domain, while the bottom displays the response function in frequency domain. The spectrum shows the vibronic progression that is expected for a monomer with a relatively large Huang-Rhys factor. This corresponds well to Figure S1 in Ref. [23] and is calculated as a test of the computer implementation.
(The "init. eigstate: 0" is administrative, denoting that the spectrum is calculated for the system in ground state (state index 0).

G Basis truncation for the homodimer

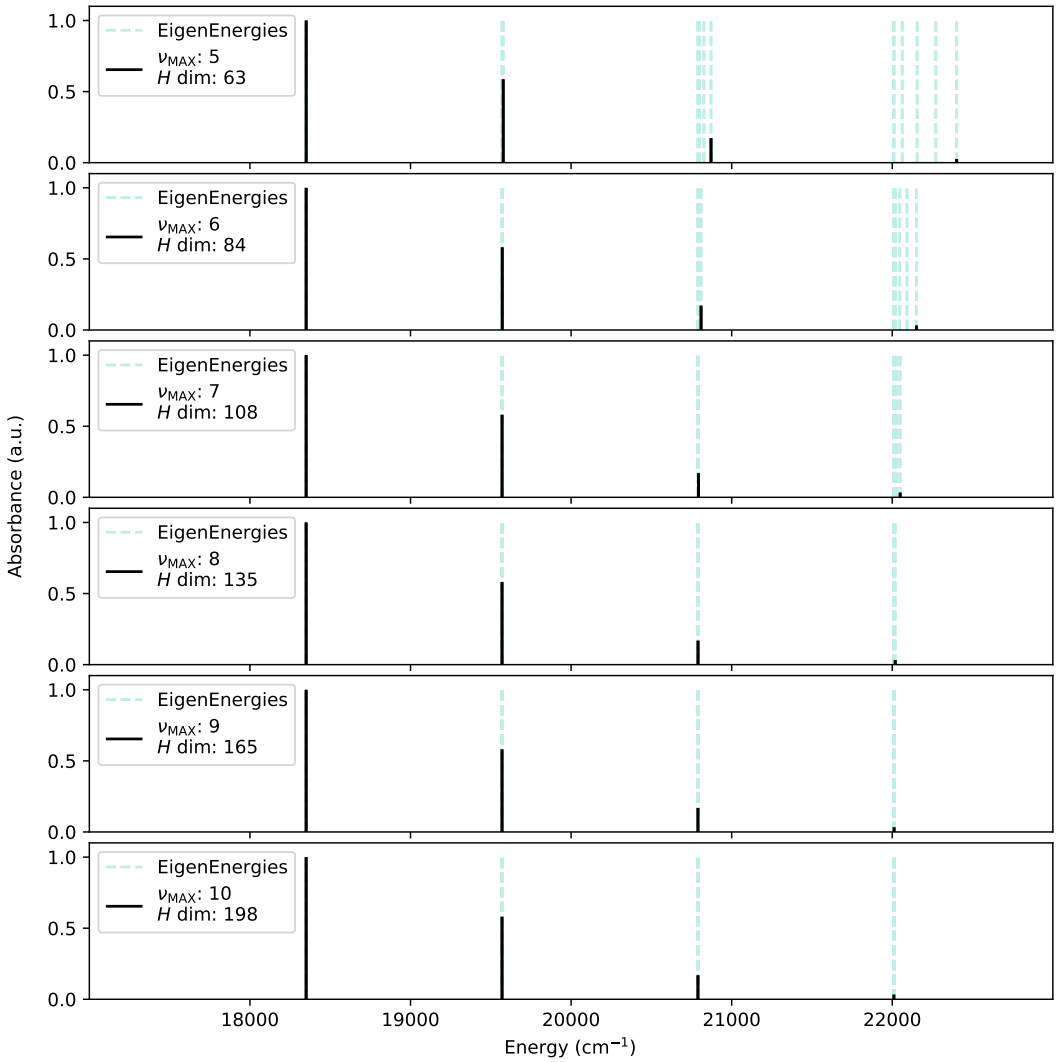

FIGURE *G1*: The stick linear absorption spectra for six different basic truncations. The dashed lines depict the system's eigenenergies at each truncation. The sticks are calculated from the electronic transition dipole moments in eigenbasis. No disorder is included in this calculation and the system temperature is zero.

The difference between these bases is the number of maximum vibrational quanta present in the system: ν_{MAX}. Note that the Hilbert space dimension 'H dim' is not proportional to ν^2_{MAX}. However, in a homodimer, the Hamiltonian size would be proportional to the square of 'one plus the maximum number of vibrational quanta per site', if the truncation would be done by limiting the number of vibrations per site, rather than the total number of vibrations in the system.

This plot helps find a compromise between computational effort and accuracy.

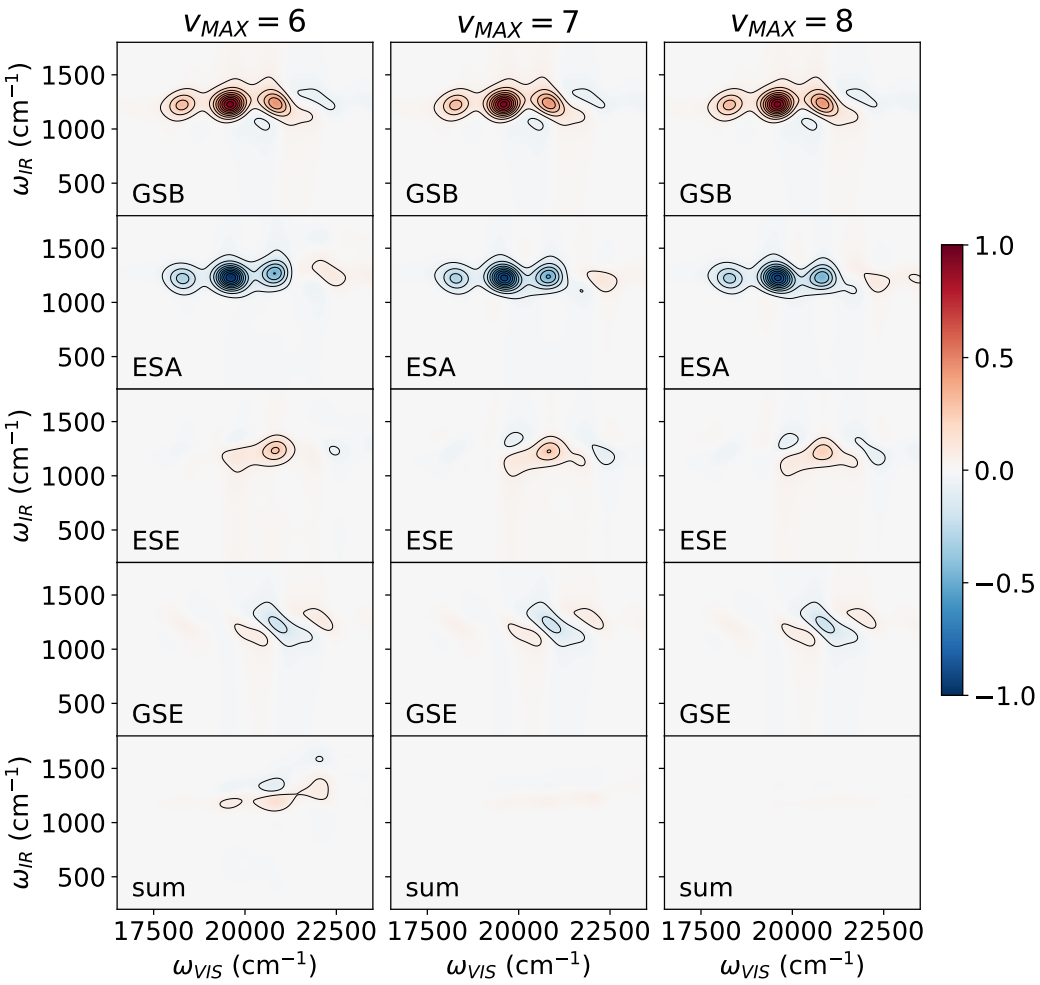

FIGURE *G2*: The comparison of 2DEV spectra for the homodimer (no disorder included) in order to investigate the artefacts introduced by basis truncation. The most noticeable feature is the fact that the different Feynman Diagrams do not add up to zero if the basis set is too small. Based on this comparison combined with the linear stick spectra seen in Fig. G1 a basis is chosen with a $\nu_{\mathrm{MAX}} = 8$